arXiv:1603.06027v4 [cond-mat.mes-hall] 31 May 2016

First-principles study of the terahertz third-order nonlinear response of metallic armchair graphene nanoribbons

Yichao Wang[1] and David R. Andersen[1, 2]

[1] *Electrical and Computer Engineering*

[2] *Physics and Astronomy*

The University of Iowa, Iowa City, IA 52242 USA

(Dated: May 25, 2016)

Abstract

We compute the terahertz third-order nonlinear conductance of metallic armchair graphene nanoribbons using time-dependent perturbation theory. Significant enhancement of the intrinsic third-order conductance over the result for instrinsic 2D single-layer graphene is observed over a wide range of temperatures. We also investigate the nonlinear response of extrinsic metallic acGNR with $|E_F| \ll 200\,\text{meV}$. We find that the third-order conductance exhibits a strong Fermi level dependence at low temperatures. A third-order critical field strength of between ~ 1 and $5\,\text{kV/m}$ is computed for the Kerr conductance as a function of temperature. For the third-harmonic conductance, the minimum critical field is computed to be $\sim 5\,\text{kV/m}$.

I. INTRODUCTION

Graphene, a monolayer of carbon atoms arranged in a 2D honeycomb lattice, has excellent electronic, mechanical, thermal and optoelectronic properties.[1] The spectrum of graphene is described by the massless Dirac equation. Due to the many unique properties of graphene, it is considered a promising material for electronic device applications.

In the terahertz (THz) to far-infrared (FIR) spectral regime, the optical conductance of graphene based systems has attracted much interest due to the ongoing search for viable THz devices. Graphene is traditionally a poor conductor in the THz to FIR spectrum, with universal conductivity $\sigma_0 = e^2/(4\hbar)$ leading to an absorption of only 2.3% at normal incidence per graphene layer.[2] However, graphene has a number of features that make it an attractive nonlinear system to study.[3–6] These include a tunable Fermi level, and more importantly a linear dispersion relation near the Dirac point.[7,8] This linear dispersion and the accompanying constant Fermi velocity v_F have led to the theoretical prediction of the generation of higher-order harmonics in graphene.[3] Mikhailov and Ziegler have developed a quasi classical kinetic theory and a quantum theory on the third order nonlinear process in graphene.[9,10] Wright *et.al.*[11] adopted a time dependent perturbation theory to analyse the linear and third order nonlinear optical response of intrinsic 2D single layer graphene (2D SLG) with an applied electric field of approximately 100 kV/m, which indicates that the strong nonlinear conductance makes graphene a potential candidate for THz photonic and optoelectronic devices. Ang *et.al.*[12,13] investigated the nonlinear optical conductivity of bilayer graphene (BLG), semihydrogenated graphene (SHG) and Kronig-Penney (KP) graphene superlattices. Gullans *et.al.*[14] studied the single photon nonlinear mechanism in graphene nanostructures and showed strong confinement of plasmons and large intrinsic nonlinearity in graphene nanostructures led to significant electric field enhancement. Recently, Mikhailov *et.al.*[15,16], Cheng *et.al.*[17–19] and Morimoto *et.al.*[20] proposed quantum theories of the third-order nonlinear response with an uniform external electric field in 2D SLG independently. This work[15–20] studies the relationship of the Fermi energy with the direct interband transition, which confirms the resonant frequencies for the third-harmonic conductance which appeared in Refs.[11,21], and the missing resonant frequencies for the Kerr conductance in Refs.[11,21] as we perform the calculations of Refs.[11,21].

Hendry *et.al.*[4] first report measurement of the coherent nonlinear optical response of single

and few-layer graphene using four-wave mixing. Their results experimentally demonstrate that graphene structures exhibits a strong nonlinear optical response in the NIR spectral region. Harmonic generation, frequency mixing, optical rectification, linear and circular photogalvanic effect, photon drag effect, photoconductivity, coherently controlled ballistic charge currents, etc. in graphene are currently the subject of intense research, and have already found a number of applications.[6] Kumar *et.al.*[22] found third harmonic generation in graphene and multi-layer graphite films grown by exfoliation. They found the nonlinear emission frequency matched well with the theoretical prediction and deducted an effective third order susceptibility on the order of $100\,\mu m^2/kV^2$. Maeng *et.al.*[23] measured the nonlinear conductivity of gate controlled graphene grown by CVD. Their work show nonlinear conductance of graphene can be efficient controlled via applied gate voltage and doping. Recently, Hafez *et.al.*[24] reported experimental results on the carrier dynamics in epitaxially grown monolayer graphene[24]. This work demonstrates that the microscopic mechanisms of nonlinear effects in graphene can be quite different from their counterparts in ordinary semiconductor systems[24]. The large nonlinear response originating from interband transitions is seven orders of magnitude stronger than the nonlinear response observed in dielectric materials without such transitions[4,25]. These theoretical and experimental studies have shown that the linear energy dispersion and high electron Fermi velocity in graphene leads to a strongly nonlinear optical response in the THz to FIR regime for various 2D graphene systems compared with the counterparts in conventional parabolic semiconductor systems.

While the nonlinear optical properties of 2D graphene structures have been studied extensively, the nonlinear optical response, which is proportional to the higher powers of the applied electric field, has been much less studied for graphene nanoribbons (GNR). Duan *et.al.*[26] studied the linear response of intrinsic metallic armchair GNR in the infrared regime with a linearly-polarized applied electric at low temperatures. Sasaki *et.al.*[27] proposed optical interband transition selection rules for acGNR with linearly-polarized electric fields in the transverse and longitudinal directions. Chung *et.al.*[28] also investigated the interband selection rules for acGNR. All of this work focused on the linear response of GNR and did not address the nonlinear response of acGNR at THz frequencies for an applied linearly-polarized electric field in the longitudinal and transverse directions.

Wang *et.al.*[29] find that thin GNRs (sub-20 nm) with smooth edges can be treated as quasi 1D quantum wires, not dominated by defects. In general, new physics (quantization

of energy, momentum *etc.*) emerges when the dimensionality of 2D graphene is reduced to a quasi 1D quantum wire. With the rapid development of techniques for the synthesis of thin GNRs[29–31], thin GNRs (sub-20 nm) may have ultra smooth edges, higher mobility and longer carrier mean free path than expected theoretically. Depending on the nature of the edges, there are two types of GNR: armchair graphene nanoribbons (acGNR) and the zigzag graphene nanoribbon (zzGNR). Electron dynamics of both acGNR and zzGNR have distinct properties, due to their geometry and boundary conditions.[32,33] Metallic acGNR exhibits a linear band structure in both tight-binding[34,35] and $\mathbf{k}\cdot\mathbf{p}$ models. Edge states contribute significantly to GNR properties, since in a nanoscale GNR, massless Dirac fermions can reach the ribbon edge within a few femtoseconds before encountering any other scattering and screening effects, such as electron-electron and electron-phonon interactions, the Peierls instability, *etc.* In general, the nonlinearity of GNR originates from the redistribution of the Dirac fermions in momentum and energy space induced by the applied electric field[6]. As a consequence, conductivity components oscillating in time and space, as well as spatially homogeneous steady state components are expected to be obtained from the resulting nonequilibrium distribution. Thus the resulting nonlinear response is sensitive to the applied field strength and polarization[6]. Therefore, it is important to study the electrodynamics for higher order harmonic generation with the existence of an applied electric field in GNR. In light of recent reports of the growth of ultra thin acGNR (sub-10 nm) reported by Kimouche *et.al.*[30] and Jacobberger *et.al.*[31], and the fact that Kimouche *et.al.*[30] show that defects (kinks) do not strongly modify the electronic structure of ultrathin acGNR, the study of the nonlinear response of these metallic acGNR is of particular significance today.

In this paper, we develop a semi-analytic approach based on the $\mathbf{k}\cdot\mathbf{p}$ approximation in the Coulomb gauge to calculate the nonlinear THz response of thin acGNR (width < 20 nm) under a moderate applied linearly-polarized electric field in the longitudinal and transverse directions. We use time dependent perturbation theory to do a Fourier analysis of the wavefunction in the presence of a strong linearly-polarized time-harmonic electric field, and obtain the linear and third-order optical THz response of thin metallic acGNR.

The paper is organized as follows. In Sec. II, we begin with the $\mathbf{k}\cdot\mathbf{p}$ approximation to obtain the time-independent wave equation and the interaction Hamiltonian with an applied electric field for acGNR, and we present a brief derivation of our semi-analytical approach to calculate the nonlinear conductance. In Sec. III, we apply our model to calculate the

nonlinear conductance of metallic acGNR. In particular, we compare the nonlinear properties of single layer metallic acGNR with those of intrinsic 2D SLG. We also propose a correction to previous work[11,21] on the third order Kerr conductance in intrinsic 2D SLG. We analyze the third-order nonlinear terms using standard definitions for these quantities: Kerr conductance for the third-order terms oscillating at frequency ω and third-harmonic conductance for the terms oscillating at frequency 3ω, determine the required applied electric field strength to induce non-negligible nonlinear effects and investigate the temperature and Fermi level dependence of the nonlinear conductance. Following this, a brief analysis of the selection rules for nonlinear THz direct interband transitions in metallic thin acGNR is discussed. Finally, the conclusions are presented in Section V.

II. MODEL

A. H_0, ψ_0 and the applied field E_μ

Graphene is a 2D hexagonal lattice (honeycomb) structure of covalently bonded carbon atoms. As there are 2 atoms per unit cell, we label them A and B respectively. At low energies, graphene carriers can be described by the massless Dirac equation. As a consequence, graphene shows a linear energy band structure near the Dirac points $\mathbf{K} = \frac{2\pi}{a_0}\left(\frac{1}{3}, \frac{1}{\sqrt{3}}\right)$ and $\mathbf{K}' = \frac{2\pi}{a_0}\left(\text{-}\frac{1}{3}, \frac{1}{\sqrt{3}}\right)$ of the Brillouin zone. Here a_0 is the triangular lattice parameter of the graphene structure.[32,33] ($a_0 = \sqrt{3}a_{cc}$ where a_{cc} is the carbon-carbon separation distance in acGNR and $a_{cc} = 1.42\,\text{Å}$).

The unperturbed $\mathbf{k}\cdot\mathbf{p}$ Hamiltonian for graphene can be written in terms of Pauli matrices as $H_{0,K} = \hbar v_F \boldsymbol{\sigma}\cdot\mathbf{k}$ for the $\mathbf{K}$ valley and $H_{0,K'} = \hbar v_F \boldsymbol{\sigma}\cdot\mathbf{k}'$ for the $\mathbf{K}'$ valley with $\mathbf{k}(\mathbf{k}')$ the perturbation from the center of the $\mathbf{K}(\mathbf{K}')$ valley. The corresponding wave functions are expressed as envelope functions $\psi_K(\mathbf{r}) = [\psi_A(\mathbf{r}), \psi_B(\mathbf{r})]$ and $\psi_{K'}(\mathbf{r}) = [\psi'_A(\mathbf{r}), \psi'_B(\mathbf{r})]$ for states near the $\mathbf{K}$ and $\mathbf{K}'$ points, respectively.

Following the development in[32,33], the time-independent (unperturbed) Hamiltonian for

a single Dirac fermion in GNR can be written as:

$$H_0 = \begin{pmatrix} H_{0,K} & 0 \\ 0 & H_{0,K'} \end{pmatrix}$$
$$= \hbar v_F \begin{pmatrix} 0 & k_x - ik_y & 0 & 0 \\ k_x + ik_y & 0 & 0 & 0 \\ 0 & 0 & 0 & -k_x - ik_y \\ 0 & 0 & -k_x + ik_y & 0 \end{pmatrix} \quad (1)$$

with wave envelope functions in the case of acGNR:

$$\psi_{n,s}(\mathbf{r}, 0) = \begin{pmatrix} \psi_{n,s}(\mathbf{r})_K \\ \psi_{n,s}(\mathbf{r})_{K'} \end{pmatrix} = \frac{e^{ik_y y}}{2\sqrt{L_x L_y}} \begin{pmatrix} e^{-i\theta_{k_n,k_y}} e^{ik_n x} \\ s e^{ik_n x} \\ -e^{-i\theta_{k_n,k_y}} e^{-ik_n x} \\ s e^{-ik_n x} \end{pmatrix} \quad (2)$$

with L_x the width of acGNR in the x (zigzag) direction, L_y the length of the acGNR in the y (armchair) direction and the direction of the isospin of the state is $\theta_{k_n,k_y} = \tan^{-1}(k_n/k_y)$.

The electronic properties of acGNR depend strongly on their width L_x. The width of acGNR can be calculated using $L_x = \frac{N}{2}a_0$, where N is the number of atoms along the zigzag edge ($\hat{x}$ direction). In general, acGNR of $N = 3M - 1$ atoms wide along the zigzag edge, with M odd, are metallic, whereas all the other cases are semiconductors[32,33]. In Fig. 1 we plot the band structure of infinitely long metallic ($L_y \to \infty$) acGNR for $N = 20$ (acGNR20). One can see that in Fig. 1 there is a Dirac point, leading to metallic behavior for a single-electron model. Thus for a width of the form $L_x = \frac{3M-1}{2}a_0$ with M odd, the allowed values of $k_n = \frac{2\pi}{3a_0}\frac{M+n}{M}$ create doubly-degenerate states for $n \neq -M$ and when $k_y \to 0$, the existence of a zero energy state indicates that the conduction and valence band touch at the Dirac points. The non-metallic bands in 1 are well above THz energies, and as a result, a THz direct interband transition can only occur between metallic subbands ($k_n = 0$) for thin metallic acGNR.

Because thin acGNR (sub-20 nm) can be treated as a quasi-1D quantum wire system[29], we have Bloch states where $k_{x,n} = \frac{2\pi}{3a_0}\frac{M+n}{M}$ and $k_{y,m} = \frac{2\pi}{L_y}m$. In metallic acGNR when $n = -M$, we can write the time-independent wave envelope function for one Dirac fermion in the lowest subband near the Dirac point, with $k_{x,n} = 0$ as:

$$\psi(\mathbf{r}, 0; m) = \phi_0(m)e^{i2\pi m y/L_y} \quad (3)$$

where $\phi_0(m)$ is found to be:

$$\phi_0(m) = \begin{bmatrix} \phi_{K,0}(m) \\ \phi_{K',0}(m) \end{bmatrix} = \frac{1}{2\sqrt{L_x L_y}} \begin{bmatrix} \mathrm{sgn}(k_y) \\ s \\ -\mathrm{sgn}(k_y) \\ s \end{bmatrix} \tag{4}$$

constructed from Eq. 2.

Let us consider metallic acGNR under an applied linearly-polarized electric field $\mathbf{E} = \hat{\mu} E_\mu e^{-i\omega t}$, of frequency ω with normal incidence. Notice that the time dependent part of the applied field $e^{-i\omega t}$ corresponds to the absorption process and $e^{i\omega t}$ corresponds to the emission process. For time-harmonic fields that turn on adiabatically[36,37] at $t \to -\infty$ and constant scalar potential $\nabla\varphi = 0$, in the Coulomb gauge[36] ($\nabla \cdot \mathbf{A} = 0$) the vector potential[11,21,36] is of the form $\mathbf{A} = \hat{\mu} E_\mu \exp(-i\omega t)/(i\omega)$ (see Appendix A for a brief discussion). The interaction with the vector potential is described by writing the canonical momentum $\mathbf{k} \to \mathbf{k} + \frac{q\mathbf{A}}{\hbar}$, where q is the elementary charge. In other words, the total Hamiltonian for graphene in the presence of a normally-incident electromagnetic field can be written as $H_K = \hbar v_F \boldsymbol{\sigma} \cdot (\mathbf{k} + \frac{q\mathbf{A}}{\hbar})$ for the $\mathbf{K}$ point and $H_{K'} = \hbar v_F \boldsymbol{\sigma} \cdot (\mathbf{k}' + \frac{q\mathbf{A}}{\hbar})$ for the $\mathbf{K}'$ point. The total Hamiltonian for acGNR can be expressed as: $H = H_0 + H_{int}$, where the interaction part of the Hamiltonian is given by:

$$H_{int} = \begin{pmatrix} H_{int,K} & 0 \\ 0 & H_{int,K'} \end{pmatrix} \tag{5}$$

with $H_{int,K(K')} = \frac{q v_F}{i\omega} \boldsymbol{\sigma} \cdot \mathbf{E_0} e^{-i\omega t}$ where $\boldsymbol{\sigma} = \hat{x}\sigma_x + \hat{y}\sigma_y$ is the Pauli matrix and $\mu = x, y$ indicates the direction of the applied linearly-polarized electric field.

B. Local conductivity and conductance

In this work, we follow Refs.[11–13,16–21,37,38] and make the relaxation-free approximation, neglecting carrier-phonon and carrier-carrier[39] scattering, defect scattering, and many body effects in our calculation. Acoustic phonon scattering may be neglected because the interaction is not phasematched due to the large (three orders of magnitude) difference between the carrier Fermi velocity v_F and the acoustic velocity. The optical phonon energy in graphene is $\sim 200\,\mathrm{meV}$ and so for low-energy carriers of the order of a few tens of meV and below, optical phonon scattering may be neglected as well. Carrier-carrier scattering increases with

the square of the carrier density. Since our model considers extrinsic metallic acGNR with Fermi energies of the order of a few meV and small excitation field strengths ($\sim 10\,\mathrm{kV/m}$), carrier-carrier scattering and many-body effects may be neglected to a good approximation. Ultrathin metallic acGNR with smooth edges have recently been fabricated showing ballistic transport due to the low defect density[30], and so it is appropriate to neglect defect scattering. Due to the block nature of the total Hamiltonian $H = H_0 + H_{int}$ in the $\mathbf{k}\cdot\mathbf{p}$ approximation, we also neglect intravalley and intervalley scattering in thin metallic acGNRs as well. Thus, the theory presented in this paper applies to low-energy (THz) carriers in thin, smooth metallic acGNR where the higher index bands ($k_{x,n} \neq 0$) are well-separated from the lowest-order linear bands (see Fig. 1).

In metallic acGNR, we describe the Dirac fermion under the influence of an applied electric field $\hat{\mu}E_\mu e^{-i\omega t}$ for the metallic band ($k_{x,n} = 0$) as an envelope wave function $\psi_\mu(\mathbf{r},t;m) = [\psi_\mu(\mathbf{r},t;m)_K, \psi_\mu(\mathbf{r},t;m)_{K'}]^T$. Using the Floquet theorem, the Fourier series expansion of $\psi_\mu(\mathbf{r},t;m)$ can be written[11–13,21,40,41] as:

$$\psi_\mu(\mathbf{r},t;m) = \sum_{l=0}^{\infty} \phi_\mu(m,l) e^{i2\pi m y/L_y} e^{\pm i\omega l t} e^{-i\epsilon t/\hbar} \tag{6}$$

with the initial condition $\phi_\mu(m,0) = \phi_0(m)$, which satisfies the requirement that when $\mathbf{A} \to 0$, $\psi_\mu(\mathbf{r},t;m)$ should be a solution of the Hamiltonian without an applied field[11–13,21,40]. The spinor $\phi_\mu(m,l)$ is given by:

$$\phi_\mu(m,l) = \begin{bmatrix} \phi_\mu(m,l)_K \\ \phi_\mu(m,l)_{K'} \end{bmatrix} = \begin{bmatrix} a_l(m) \\ b_l(m) \\ c_l(m) \\ d_l(m) \end{bmatrix} \tag{7}$$

We can then calculate the charge density as: $\rho = |\psi_\mu(\mathbf{r},t;m)|^2$, where the particle density operator is $\rho_{op}(\mathbf{r}) = \delta(\mathbf{r} - \mathbf{r_{op}})$. After applying the continuity equation $q\frac{\partial \rho}{\partial t} + \nabla \cdot \mathbf{j} = 0$, along with the Schrödinger equation $H\psi_\mu(\mathbf{r},t;m) = i\hbar\frac{\partial \psi_\mu(\mathbf{r},t;m)}{\partial t}$ under the Coulomb gauge, we obtain the local (single-particle) current density for Dirac fermions in the metallic sub-band of acGNR:

$$\mathbf{j}(m,t) = \hat{x} j_x(m,t) + \hat{y} j_y(m,t) \tag{8}$$

with the local current density component defined as:

$$j_\nu(m,t) = q\psi_\mu(\mathbf{r},t;m)^\dagger \frac{\partial H}{\hbar \partial k_\nu} \psi_\mu(\mathbf{r},t;m) \tag{9}$$

where $\mu = x, y$ indicates the direction of the polarization of the applied electric field, and $\nu = x, y$ indicates the component of the induced current. After substituting Eq. (6) into Eq. (9), the Fourier series expansion of the local current density becomes:

$$\begin{aligned}
j_\nu(m,t) =& q\left[\phi_\mu(m,0) + \phi_\mu(m,1)e^{-i\omega t} + \phi_\mu(m,2)e^{-i2\omega t} + \cdots\right]^\dagger \\
&\times \frac{\partial H}{\hbar \partial k_\nu}\left[\phi_\mu(m,0) + \phi_\mu(m,1)e^{-i\omega t} + \phi_\mu(m,2)e^{-i2\omega t} + \cdots\right] \\
=& q\Bigg\{\left[\phi_\mu^\dagger(m,0)\frac{\partial H}{\hbar\partial k_\nu}\phi_\mu(m,0) + \phi_\mu^\dagger(m,1)\frac{\partial H}{\hbar\partial k_\nu}\phi_\mu(m,1) + \cdots\right] \\
&+ e^{-i\omega t}\left[\phi_\mu^\dagger(m,0)\frac{\partial H}{\hbar\partial k_\nu}\phi_\mu(m,1) + \phi_\mu^\dagger(m,1)\frac{\partial H}{\hbar\partial k_\nu}\phi_\mu(m,2) + \cdots\right] \\
&+ e^{+i\omega t}\left[\phi_\mu^\dagger(m,1)\frac{\partial H}{\hbar\partial k_\nu}\phi_\mu(m,0) + \phi_\mu^\dagger(m,2)\frac{\partial H}{\hbar\partial k_\nu}\phi_\mu(m,1) + \cdots\right] \\
&+ e^{-i2\omega t}\left[\phi_\mu^\dagger(m,0)\frac{\partial H}{\hbar\partial k_\nu}\phi_\mu(m,2) + \phi_\mu^\dagger(m,1)\frac{\partial H}{\hbar\partial k_\nu}\phi_\mu(m,3) + \cdots\right] \\
&+ e^{+i2\omega t}\left[\phi_\mu^\dagger(m,2)\frac{\partial H}{\hbar\partial k_\nu}\phi_\mu(m,0) + \phi_\mu^\dagger(m,3)\frac{\partial H}{\hbar\partial k_\nu}\phi_\mu(m,1) + \cdots\right] \\
&+ e^{-i3\omega t}\left[\phi_\mu^\dagger(m,0)\frac{\partial H}{\hbar\partial k_\nu}\phi_\mu(m,3) + \cdots\right] \\
&+ e^{+i3\omega t}\left[\phi_\mu^\dagger(m,3)\frac{\partial H}{\hbar\partial k_\nu}\phi_\mu(m,0) + \cdots\right] + \cdots\Bigg\}
\end{aligned} \tag{10}$$

In general, for the study of third-order nonlinear optical processes induced by an arbitrary superposition of three time-harmonic electric fields, it is customary to write the local current density due to an individual atom as the product of a fourth-rank conductivity tensor with the three arbitrary applied fields. In the current work, we consider a much simpler case. The applied electric field is linearly-polarized along the longitudinal armchair (transverse zigzag) or $\hat{y}$ ($\hat{x}$) direction and has a single frequency ω. As a result, the expression for the local current density can be written[16]:

$$\begin{aligned}
j_\nu(m,t) &= \left[e^{-i\omega t}\tilde{\sigma}^{(1)}_{\mu\nu}(\omega)E_\mu + 3e^{-i\omega t}\tilde{\sigma}^{(3)}_{\nu\mu\mu\mu}(\omega,\omega,-\omega)E_\mu^3 + e^{-i3\omega t}\tilde{\sigma}^{(3)}_{\nu\mu\mu\mu}(\omega,\omega,\omega)E_\mu^3 + \cdots\right] + c.c. \\
&= \left[j_\nu^{(1)}(m,\omega,t) + j_\nu^{(3)}(m,\omega,t) + j_\nu^{(3)}(m,3\omega,t) + \ldots\right] + c.c.
\end{aligned} \tag{11}$$

By matching term-by-term the expansions in Eqs. 10 and 11, we can obtain the individual non-zero elements in the local third-order conductivity tensor. Further, by rewriting Eq. 11, we see that the expressions for the Fourier components of the local current density reduce to terms involving a local 2×2 conductivity matrix and the applied electric field[11–13,21]:

$$j_\nu^{(i)}(m,\omega_0) = \sigma^{(i)}_{\mu\nu}(m,\omega_0)E_\mu e^{-i\omega_0 t} \tag{12}$$

where for $i = 1$, $\omega_0 = \omega$; and for $i = 3$, $\omega_0 = \omega$ ($\omega_0 = 3\omega$) for the Kerr (third-harmonic) terms in the local current density expansion, and where $\sigma^{(i)}_{\mu\nu}(m, \omega_0)$ is the local ith-order conductivity matrix defined as for 2D SLG in Refs.[11–13,21,25,40–42]

To compute the *total* current density, we sum over all possible states, using the thermal distribution $N(\epsilon, E_F) = n_F(-|\epsilon|, E_F) - n_F(|\epsilon|, E_F)$ where $|\epsilon| = |m|hv_F/L_y$. The total current density[11–13,21,25,40–42] is therefore:

$$J_\nu(t) = g_s\, g_v \sum_m j_\nu(m, t) N(\epsilon, E_F) \tag{13}$$

with g_s, $g_v = 2$ the spin and valley degeneracies respectively. Here the initial occupancy of the system is described by the Fermi function $n_F(\epsilon, E_F)$. Conduction band states are occupied with probability $n_F(|\epsilon|, E_F)$ and valence band states are occupied with probability $n_F(-|\epsilon|, E_F)$. The Brey-Fertig wavefunction of Eqs. (3) and (4) is normalized over the entire sample[32,33], implying that the states at k_y for each valley are occupied with probability 1/2 (assumes N carriers per unit cell). Since there are $2N$ carriers per unit cell, we multiply by $g_v = 2$ to include the contribution to the total current from all $2N$ carriers. As the local current density $j_\nu(m, t)$ conserves charge current density[37,43,44] with an applied vector potential $\mathbf{A}$ and the symmetry of graphene, it is straightforward to expand the total current component $J_\nu(t)$ as Fourier series of odd higher-harmonics[3,4,9–13,15–19,21,40]. Again, following Refs.[16], we write the total current density as:

$$\begin{aligned} J_\nu(t) &= \left[e^{-i\omega t}\sigma^{(1)}_{\mu\nu}(\omega)E_\mu + 3e^{-i\omega t}\sigma^{(3)}_{\nu\mu\mu\mu}(\omega, \omega, -\omega)E^3_\mu + e^{-i3\omega t}\sigma^{(3)}_{\nu\mu\mu\mu}(\omega, \omega, \omega)E^3_\mu + \cdots\right] + c.c. \\ &= \left[J^{(1)}_\nu(\omega, t) + J^{(3)}_\nu(\omega, t) + J^{(3)}_\nu(3\omega, t) + \cdots\right] + c.c \end{aligned} \tag{14}$$

Adopting the notation in Refs.[11–13,21,27], we define the ith-order conductance component[11–13,21] as a 2×2 conductance matrix relating the total nonlinear current density and the applied linearly-polarized electric field:

$$J^{(i)}_\nu(\omega_0, t) = g^{(i)}_{\mu\nu}(\omega_0)E_\mu e^{-i\omega_0 t} \tag{15}$$

For the metallic band in thin acGNR, with an applied a $\hat{y}$-polarized electric field $\hat{y}E_y e^{-i\omega t}$,

the Hamiltonian H for $k_y = 2\pi m/L_y$ can be written as:

$$H = H_0 + H_{int}$$
$$= \hbar v_F \begin{pmatrix} 0 & -i(k_y + \frac{eE_y}{i\hbar\omega}e^{-i\omega t}) & 0 & 0 \\ +i(k_y + \frac{eE_y}{i\hbar\omega}e^{-i\omega t}) & 0 & 0 & 0 \\ 0 & 0 & 0 & -i(k_y + \frac{eE_y}{i\hbar\omega}e^{-i\omega t}) \\ 0 & 0 & +i(k_y + \frac{eE_y}{i\hbar\omega}e^{-i\omega t}) & 0 \end{pmatrix} \tag{16}$$

We then proceed to solve the Schrödinger equation $H\psi_\mu(\mathbf{r}, t; m) = i\hbar\frac{\partial}{\partial t}\psi_\mu(\mathbf{r}, t; m)$. Due to the orthogonal properties of the basis sets $\{e^{-il\omega t}\}$, we obtain the following recursion relations for the spinor components:

$$(\epsilon + n\hbar\omega)a_l(m) = \hbar(-ik_y)b_l(m) - \frac{ev_F E_y}{\omega}b_{l-1}(m) \tag{17a}$$
$$(\epsilon + n\hbar\omega)b_l(m) = \hbar(+ik_y)a_l(m) + \frac{ev_F E_y}{\omega}a_{l-1}(m) \tag{17b}$$
$$(\epsilon + n\hbar\omega)c_l(m) = \hbar(-ik_y)d_l(m) - \frac{ev_F E_y}{\omega}d_{l-1}(m) \tag{17c}$$
$$(\epsilon + n\hbar\omega)d_l(m) = \hbar(+ik_y)c_l(m) + \frac{ev_F E_y}{\omega}c_{l-1}(m) \tag{17d}$$

For the lowest band in metallic acGNR, the energy of the carriers in the absence of an applied electric field is $-\hbar v_F|k_y|$. Following this procedure, we arrive at the following local current density terms defined in Eq. (12):

$$j_y^{(1)}(m,\omega) = qv_F\left[i\left(a_1(m)b_0^\dagger(m) - a_0^\dagger(m)b_1(m)\right) + i\left(c_1(m)d_0^\dagger(m) - c_0^\dagger(m)d_1(m)\right)\right] \tag{18a}$$
$$j_y^{(3)}(m,\omega) = qv_F\left[i\left(a_2(m)b_1^\dagger(m) - a_1^\dagger(m)b_2(m)\right) + i\left(c_2(m)d_1^\dagger(m) - c_1^\dagger(m)d_2(m)\right)\right] \tag{18b}$$
$$j_y^{(3)}(m,3\omega) = qv_F\left[i\left(a_3(m)b_0^\dagger(m) - a_0^\dagger(m)b_3(m)\right) + i\left(c_3(m)d_0^\dagger(m) - c_0^\dagger(m)d_3(m)\right)\right] \tag{18c}$$
$$j_x^{(1)}(m,\omega) = qv_F\left[\left(a_1(m)b_0^\dagger(m) + a_0^\dagger(m)b_1(m)\right) - \left(c_1(m)d_0^\dagger(m) + c_0^\dagger(m)d_1(m)\right)\right] \tag{18d}$$
$$j_x^{(3)}(m,\omega) = qv_F\left[\left(a_2(m)b_1^\dagger(m) + a_1^\dagger(m)b_2(m)\right) - \left(c_2(m)d_1^\dagger(m) + c_1^\dagger(m)d_2(m)\right)\right] \tag{18e}$$
$$j_x^{(3)}(m,3\omega) = qv_F\left[\left(a_3(m)b_0^\dagger(m) + a_0^\dagger(m)b_3(m)\right) - \left(c_3(m)d_0^\dagger(m) + c_0^\dagger(m)d_3(m)\right)\right] \tag{18f}$$

We make the relaxation-free approximation, neglecting all scattering effects as discussed above. We introduce an infinitesimal broadening factor[11,16–20,37,38] Γ, by making the substitution $\omega = \omega + i\Gamma$ in the $\phi_\mu(m, l)$ spinor. The ith-order local nonlinear conductivity $\sigma_{\mu\nu}^{(i)}(m, \omega_0)$ is then obtained from Eq. (12) and summing over all states, with the Fermi

energy E_F, $k_y = 2\pi m/L_y$ and $\omega_y = v_F k_y$, we obtain the nonlinear conductance as:

$$\begin{aligned} g^{(i)}_{\mu\nu}(\omega_0) &= \lim_{\Gamma\to 0} g_s g_v \sum_{m=-\infty}^{\infty} \sigma^{(i)}_{\mu\nu}(m,\omega_0) N(\omega_y, E_F) \\ &= \lim_{\Gamma\to 0} g_s g_v \frac{L_y}{2\pi} \int_{-\infty}^{\infty} dk_y\, \sigma^{(i)}_{\mu\nu}(m,\omega_0) N(\omega_y, E_F) \end{aligned} \tag{19}$$

where the thermal factor in Eq. (19) is:

$$N(\omega_y, E_F) = n_F(-\hbar|\omega_y|, E_F) - n_F(\hbar|\omega_y|, E_F) = \frac{\sinh[\hbar|\omega_y|/(k_B T)]}{\cosh[E_F/(k_B T)] + \cosh[\hbar|\omega_y|/(k_B T)]} \tag{20}$$

III. RESULTS AND DISCUSSION

In what follows, we summarize the characteristics of the nonlinear conductance for all combinations of applied field polarization and current direction.

A. E_x

If the applied electric field **E** is linearly polarized along the transverse direction of the acGNR ($\hat{x}$ direction), for the metallic band where $k_{x,n} = 0$, a net zero local current density for the $j_x(m,t)$ and $j_y(m,t)$ components is obtained. This result implies there is neither linear nor third-order nonlinear current in metallic acGNR when an electric field polarized transverse to the longitudinal direction of the acGNR is applied.

B. E_y

For the case where the applied electric field **E** is linearly polarized along the longitudinal direction of the acGNR ($\hat{y}$ direction), for metallic band where $k_{x,n} = 0$, we arrive at the following expressions for the isotropic nonlinear conductance:

$$\begin{aligned} g^{(1)}_{yy}(\omega) &= g_0 \frac{g_s g_v v_F}{\omega L_x} \left[-N(\frac{\omega}{2}, E_F) \right] \\ g^{(3)}_{yy}(\omega) &= g_0 \frac{e^2 E_y^2 v_F^2}{\hbar^2 \omega^4} \frac{g_s g_v v_F}{\omega L_x} \left[-2N(\frac{\omega}{2}, E_F) - N(\omega, E_F) \right] \\ g^{(3)}_{yy}(3\omega) &= g_0 \frac{e^2 E_y^2 v_F^2}{\hbar^2 \omega^4} \frac{g_s g_v v_F}{\omega L_x} \left[\frac{1}{2} N(\frac{\omega}{2}, E_F) - N(\omega, E_F) + \frac{1}{2} N(\frac{3\omega}{2}, E_F) \right] \end{aligned} \tag{21}$$

and the anisotropic nonlinear conductance:

$$
\begin{aligned}
g^{(1)}_{yx}(\omega) &= g_0 \frac{g_s g_v v_F}{\omega L_x} \left[N(\frac{\omega}{2}, E_F) \right] \\
g^{(3)}_{yx}(\omega) &= g_0 \frac{e^2 E_y^2 v_F^2}{\hbar^2 \omega^4} \frac{g_s g_v v_F}{\omega L_x} \left[N(\omega, E_F) \right] \\
g^{(3)}_{yx}(3\omega) &= g_0 \frac{e^2 E_y^2 v_F^2}{\hbar^2 \omega^4} \frac{g_s g_v v_F}{\omega L_x} \left[-\frac{1}{2} N(\frac{\omega}{2}, E_F) + N(\omega, E_F) - \frac{1}{2} N(\frac{3\omega}{2}, E_F) \right]
\end{aligned}
\tag{22}
$$

with the $N(\omega)$ defined in Eq. (20), and the quantum conductance $g_0 = \frac{e^2}{4\hbar}$. Due to the inversion symmetry inherent in acGNR, the *2*nd-order current makes no contribution to the total current.

In the discussion below, we compare our results for the nonlinear conductance of metallic acGNR with those reported by Wright, *et.al.*[11] and Ang *et.al.*[21] for intrinsic 2D SLG. In Eq. 70 of Ang *et.al.*[21], they write the expression for the third-order Kerr conductance as:

$$
g^{(3)}(\omega)_{2D} = -g_0 \frac{e^2 E_0^2 v_F^2}{\hbar^2 \omega^4} \left[2 \tanh \left(\frac{\hbar \omega}{2 k_B T} \right) \right] \tag{23}
$$

We believe this expression omits an additional required term due to the resonance at $\epsilon = \hbar\omega/2$. The correct expression for the third-order Kerr conductance is:

$$
g^{(3)}(\omega)_{2D} = -g_0 \frac{e^2 E_0^2 v_F^2}{\hbar^2 \omega^4} \left[\frac{5}{4} N \left(\frac{\omega}{2}, E_F \right) + 2 N(\omega, E_F) \right] \tag{24}
$$

Notice that for intrinsic 2D SLG ($E_F = 0$), $N(\omega, 0) = \tanh\left[\hbar|\omega|/(2k_BT)\right]$, and we recover the thermal factor used in Refs.[11,21]. The missing $\frac{5}{4}N(\frac{\omega}{2})$ term in Eq. 23 is the missing contribution for $|\epsilon| = \hbar\omega/2$. As both $\epsilon = \pm\hbar\omega/2$ and $\epsilon = \pm\hbar\omega$ contribute to the generation of the third-order Kerr current[16,17,19], we believe that Eq. 24 is correct. At $T = 0\,\mathrm{K}$, the real part of the Kerr conductance has two threshold frequencies, $\omega = \pm 2E_F/\hbar$ and $\omega = \pm E_F/\hbar$, corresponding to the contribution for states with energies $\epsilon = \pm\hbar\omega/2$ and $\pm\epsilon = \hbar\omega$, or the resonant transitions for which the Fermi level gap $2|E_F/\hbar|$ matches the one photon and two photon frequencies respectively[17,19]. We note that the zero temperature result of Refs.[15–20] contain the same threshold frequencies. As a result, the N-photon coupling approach we have adopted[11,21] here and the quantum theories of the third-order nonlinear response[15–20] show qualitative agreement. The position of the peaks shown in the plots of Refs[16–19] in the absence of broadening are at the threshold frequencies with respect to $E_F/\hbar$ derived from Eq. (24) at $T = 0\,\mathrm{K}$. Therefore, we compute $g^{(3)}(\omega)$ for 2D SLG using Eq. (24) in what follows.

In Eq. (71) of Ang *et.al.*[21], they write the expression for the third-order third-harmonic conductance as:

$$g^{(3)}(3\omega)_{2D} = g_0 \frac{e^2 E_0^2 v_F^2}{\hbar^2 \omega^4} \left[\frac{13}{48} \tanh(\frac{\hbar\omega}{4k_B T}) - \frac{2}{3} \tanh(\frac{\hbar\omega}{2k_B T}) + \frac{45}{48} \tanh(\frac{3\hbar\omega}{4k_B T}) \right] \tag{25}$$

Our analysis of the problem gives the same set of coefficients as Eq. (25), to wit:

$$g^{(3)}(3\omega)_{2D} = g_0 \frac{e^2 E_0^2 v_F^2}{\hbar^2 \omega^4} \left[\frac{13}{48} N(\frac{\omega}{2}, E_F) - \frac{2}{3} N(\omega, E_F) + \frac{45}{48} N(\frac{3\omega}{2}, E_F) \right] \tag{26}$$

For intrinsic 2D SLG ($E_F = 0$), $N(\omega, 0) = \tanh\left[\hbar|\omega|/(2k_B T)\right]$, and therefore Eq. (26) reduces to Eq. (25) used in Refs.[11,21]. As a result, we compute $g^{(3)}(3\omega)$ for intrinsic 2D SLG using Eq. (26) in what follows. The three threshold frequencies in Eq. (26) are the same as those obtained by Morimoto *et.al.*[20]. At $T = 0\,\mathrm{K}$, the resonant frequencies are $\omega = \pm 2E_F/\hbar$, $\omega = \pm E_F/\hbar$ and $\omega = \pm 2E_F/3\hbar$, corresponding to the contribution for states at $\epsilon = \pm\hbar\omega/2$, $\epsilon = \pm\hbar\omega$ and $\epsilon = \pm 3\hbar\omega/2$, or the resonant transitions for which the Fermi level gap $2|E_F/\hbar|$ matches the frequencies of the one photon, two photon, and three photon transitions respectively[17,19]. Interestingly, the coefficients for $\omega/2$, ω and $3\omega/2$ for the third-harmonic expression in Refs.[17–19], are $17/48$, $-4/3$ and $45/48$ respectively. As Mikhailov pointed out, different theories of the THz nonlinear response in 2D SLG may show somewhat contradictory[16] results, the difference between these coefficients being due to the extreme complexity of the problem. However, we point out that Eq. (26) shows that the main contribution for third-harmonic conductance is from the $3\omega/2$ resonance. This observation is confirmed by the results from three independent models: Wright *et.al.*[11], Mikhailov[16] and Cheng *et.al.*[17–19].

A thorough analysis of our objection to the Wright *et.al.*[11] and Ang *et.al.*[21] calculation of the Kerr conductance for intrinsic 2D SLG is provided in the Appendix below.

The total third-order nonlinear current for metallic acGNR can be expressed as:

$$J_\nu^{(3)}(t) = g_{y\nu}^{(3)}(\omega) E_y e^{-i\omega t} + g_{y\nu}^{(3)}(3\omega) E_y e^{-i3\omega t} + c.c. \tag{27}$$

This result shows that for metallic acGNR, the third-order nonlinear current is a superposition of two frequency terms: (i) $g_{y\nu}^{(3)}(\omega)$, the third-order Kerr conductance, which has a single frequency electron current density term corresponding to the absorption of two photons and the simultaneous emission of one photon; and (ii), $g_{y\nu}^{(3)}(3\omega)$, the third-order third-harmonic conductance term corresponding to the simultaneous absorption of three photons. The complex conjugate parts in Eq. 27 are for the emission process.

In this paper we consider the case where the length of the ribbon $L_y \to \infty$, and as a result, we have a quasi continuum of states for the linear bands near the Dirac points in metallic acGNR. To simplify the discussion, we present results for acGNR20, the armchair graphene nanoribbon $N = 20$ atoms wide.

Figs. 2-7 present results computed using our model described in Section II. Fig. 2 summarizes the comparison between the results for intrinsic 2D SLG and acGNR, indicating that at low temperatures, the isotropic third-order Kerr conductances is significantly larger than for 2D SLG. At $T = 0\,\mathrm{K}$, the third-order third-harmonic conductance is zero. The room temperature Kerr conductance continues to be signficantly larger, and the third-harmonic conductance becomes of the order of that for 2D SLG. Fig. 3 describes both the temperature and width dependence of the third-order conductances for thin, metallic acGNR. The decay with increasing temperature for the acGNR Kerr conductances are similar to that of 2D SLG, with the acGNR conductances maintaining their significantly larger relative size. For the third-harmonic conductances, quite different behavior is observed; the acGNR third-harmonic conductance is 0 at $T = 0\,\mathrm{K}$, increases to a maximum, and then decays much faster than for 2D SLG with further increases in temperature. The decay rate as a function of width for all acGNR third-order conductances is observed to follow a simple width dependence rule discussed below.

Fig. 4 describes the temperature dependence of the field strength required for the nonlinear conductance to dominate over the linear conductance. Results indicate that this critical field is quite small, varying from $1 - 5\,\mathrm{kV/m}$ for the third-order Kerr conductance, and exhibiting a minimum of $\sim 5\,\mathrm{kV/m}$ for the third-order third-harmonic conductance. Figs. 5 and 6 illustrate several novel features of the Kerr and third-harmonic conductances for *extrinsic* acGNR as a function of temperature. For the Kerr conductance, an antiresonance develops at low temperature and broadens with increasing E_F. For the third-harmonic nonlinearity, the antiresonance found at $T = 0\,\mathrm{K}$ for intrinsic acGNR is seen to shift to higher temperatures as E_F increases.

Finally, Fig. 7, illustrates the behavior of the third-order Kerr and third-harmonic nonlinearities for extrinsic acGNR as a function of excitation frequency $\omega = 2\pi f$. Most remarkably, the third-harmonic nonlinearity is non-zero over a finite bandwidth at $T = 0\,\mathrm{K}$; a result of the state-blocking that occurs in extrinsic material. The excitation-frequency dependence of the nonlinear conductances at room temperature is also show. In the discussion that follows,

we investigate each of these features in more detail.

The frequency dependent nonlinear conductance in units of $g_0 = e^2/4\hbar$ for intrinsic acGNR20, calculated assuming an applied field strength of 10 kV/m, is plotted in Fig. 2, together with the third-order Kerr conductance of 2D SLG. Both nonlinear terms for intrinsic metallic acGNR20 and 2D SLG decrease rapidly with frequency. The huge nonlinearities at lower frequencies are associated with the strong interaction of carriers with low energy photons. The third-order Kerr conductance, $g^{(3)}_{y\nu}(\omega)$ for acGNR20 is approximately three orders of magnitude larger than that for 2D SLG. The exact enhancement factor for nonlinear conductances in metallic acGNR is a function of the nanoribbon width, and from Eqs. 21, 22 is determined to be $v_F/\omega Lx$. Due to the thermal factor cancellation in the expression for the nonlinear third-harmonic conductance, $g^{(3)}_{y\nu}(3\omega)$ tends to be much less than $g^{(3)}_{y\nu}(\omega)$. When $T = 0\,\mathrm{K}$, the third-harmonic conductance is zero for intrinsic acGNR20. For $T = 300\,\mathrm{K}$, the third-harmonic conductance is of the same order as for 2D SLG.

In Fig. 3, we illustrate the temperature and width dependence of the third-order nonlinear conductance for intrinsic metallic acGNR and 2D SLG for an excitation frequency of 1 THz and an applied field strength of 10 kV/m. In Figs. 3a and 3b, $g^{(3)}_{y\nu}(\omega)$ is shown to decrease monotonically with temperature T. However, $g^{(3)}_{y\nu}(3\omega)$ is initially zero at $T = 0\,\mathrm{K}$ and increases to its maximum value (~ 2 orders of magnitude above that for 2D SLG) at approximately $T = 17\,\mathrm{K}$ (the exact location of the maximum is a function of the thermal factor appearing in the expressions for the conductance). It then decreases at a faster rate then $g^{(3)}_{y\nu}(\omega)$ for $T > 17\,\mathrm{K}$. The rate of decrease with temperature for $g^{(3)}_{y\nu}(\omega)$ is approximately the same as for 2D SLG.

In Figs. 3c and 3d we see that both third-order nonlinear conductance components are inversely proportional to the width of the acGNR L_x. This dependence of the conductance on L_x is due to the unitless factor $v_F/\omega L_x$ in Eqs. 21, 22, which implies that the total quasi-1D nonlinear current is constant and invariant of the nanoribbon width. We see that for $L_x \simeq 20\,\mathrm{nm}$, or acGNR164, $g^{(3)}_{y\nu}(\omega)$ is still greater than that of 2D SLG for an excitation frequency of 1 THz, which again suggests that thin metallic acGNR ($L_x \leqslant 20\,\mathrm{nm}$) manifests a much stronger Kerr conductance $g^{(3)}_{y\nu}(\omega)$ than 2D SLG over a wide range of widths. These findings suggest that metallic acGNR of submicron width is a better candidate than 2D SLG for nonlinear THz device applications.

In order to evaluate the frequency-conversion device potential of metallic acGNR, we

define a critical field strength $E^{(3)}_{c,y\nu}(\omega,T)$ as the field strength when the nonlinear conductance dominates over the linear conductance ($|g^{(3)}_{y\nu}|/g_0 > 1$ where $g_0 = e^2/4\hbar$). In Fig. 4 we plot the temperature dependence of the critical field strength for intrinsic metallic acGNR assuming a 1 THz excitation frequency. Fig. 4a illustrates the change in critical field as a function of temperature for both intrinsic metallic acGNR and 2D SLG. Due to the thermal factor cancellation, at low temperatures, the third-order conductance $g^{(3)}_{y\nu}(3\omega)$ for acGNR20 exhibits a larger critical field strength than 2D SLG. As the thermal distribution broadens with increasing T, the critical strength drops to 10% of the critical field strength for 2D SLG. As the temperature rises further, $E^{(3)}_{c,y\nu}(3\omega,T)$ increases until it rises above that for 2D SLG near $T = 170\,\mathrm{K}$ again. For the Kerr conductance term, the critical field $E^{(3)}_{c,y\nu}(\omega,T)$, increases as temperature increases, but it stays ~ 1 order of magnitude below the critical field for 2D SLG. Further, the relatively small change in critical field for $g^{(3)}_{y\nu}(\omega)$ from $T = 0\,\mathrm{K}$ to $T = 300\,\mathrm{K}$ indicates that metallic acGNR should exhibit excellent frequency conversion efficiencies for the optical Kerr process. The critical field strength we obtained is much smaller than the damage threshold[25], the strong nonlinear response, or the small values of the critical field exhibited by metallic acGNR for both Kerr and third-harmonic nonlinearities suggest that, low THz and low doped metallic acGNR are preferable to exploit the nonlinearity at intensities below the damage threshold[45]. As a result, low dopend thin metallic acGNR will be excellent for use in the fabrication of nonlinear optical frequency-conversion devices[4,25].

In Figs. 5 and 6 we study the Kerr $g^{(3)}_{y\nu}(\omega)$ and third-harmonic $g^{(3)}_{y\nu}(3\omega)$ conductances as a function of the Fermi level E_F (since the behavior of the system is symmetric for E_F about $E_F = 0$ in Figs. 5a and 6a, we only plot results for positive E_F). For E_F well below the optical phonon energy ($\sim 200\,\mathrm{meV}$), we plot the Fermi-level dependence of $g^{(3)}_{y\nu}(\omega)$ and $g^{(3)}_{y\nu}(3\omega)$ assuming a 1 THz excitation at $T = 0\,\mathrm{K}$ and $T = 300\,\mathrm{K}$. Perhaps the most important observations are for the 0 K case. We see three threshold frequencies for E_F/h: 0.5 THz, 1 THz and 1.5 THz. These frequencies correspond to turning on/off the thermal distribution[16–19] at $\omega/2$, ω and $3\omega/2$. We note that $g^{(3)}_{y\nu}(3\omega)$ is nonzero over the $\omega/2$ to $3\omega/2$ doping window. In this window, only the $N(\omega)$ thermal factor term contributes to the $g^{(3)}_{y\nu}(3\omega)$ transition. Near room temperature, there are always electron and hole states[17–19] in the energy range determined by the thermal factor. As a result, we always observe nonzero conductance at all non-zero temperatures. This result suggests that at low temperatures, light doping will greatly enhance $g^{(3)}_{y\nu}(3\omega)$. But the enhancement we observe

at low temperature for $g^{(3)}_{y\nu}(3\omega)$ disappears near room temperature. Also, the curves for different values of E_F asymptotically approach the intrinsic acGNR conductance, as the temperature increases.

In Fig. 7, we compare the conductances $g^{(3)}_{y\nu}(\omega)$ and $g^{(3)}_{y\nu}(3\omega)$ of extrinsic acGNR20 ($E_F/h = 0.7\,\mathrm{THz}$) for different temperatures and with the corresponding values for intrinsic 2D SLG. For the $T = 0\,\mathrm{K}$ case, we observe a sharp onset for both the isotropic and anisotropic Kerr conductances at E_F/h ($\omega/2\pi = 0.7\,\mathrm{THz}$) and a further increase at $2E_F/h$ ($\omega/2\pi = 1.4\,\mathrm{THz}$) for the isotropic Kerr conductance. These changes are due to different terms in the thermal factor turning on at these excitation frequencies (see Table I).

The third-harmonic result is significantly different at $T = 0\,\mathrm{K}$. In this case the conductance turns on abruptly at $2E_F/3h$ ($\omega/2\pi = 0.467\,\mathrm{THz}$) and turns off abruptly at $2E_F/h$ ($\omega/2\pi = 1.4\,\mathrm{THz}$). These changes are also due to the relevant terms in the thermal factor turning on at particular excitation frequencies (see Table I).

TABLE I. Thermal Factor Terms for excitation frequency ω (*cf.* Eqs. 21, 22)

Kerr Conductance ($T = 0\,\mathrm{K}$)	
Frequency Range	Thermal Factor Terms
$0 < \omega \leq E_F/\hbar$	all terms are 0
$E_F/\hbar < \omega \leq 2E_F/\hbar$	$N(\omega, E_F) = 1$
$\omega > 2E_F/\hbar$, isotropic	$2N(\omega/2, E_F) + N(\omega, E_F) = 3$
$\omega > 2E_F/\hbar$, anisotropic	$N(\omega, E_F) = 1$
Third-harmonic Conductance ($T = 0\,\mathrm{K}$)	
Frequency Range	Thermal Factor Terms
$0 < \omega \leq 2E_F/3\hbar$	all terms are 0
$2E_F/3\hbar < \omega \leq E_F/\hbar$	$-\frac{1}{2}N(3\omega/2, E_F) = -\frac{1}{2}$
$E_F/\hbar < \omega \leq 2E_F/\hbar$	$N(\omega, E_F) - \frac{1}{2}N(3\omega/2, E_F) = \frac{1}{2}$
$\omega > 2E_F/\hbar$	$-\frac{1}{2}N(\omega/2, E_F) + N(\omega, E_F) - \frac{1}{2}N(3\omega/2, E_F) = 0$

For $T = 300\,\mathrm{K}$, we note that the extrinsic Kerr conductance is strongly enhanced over intrinsic 2D SLG, as it is in the intrinsic case. Further, the extrinsic third-harmonic conductance is of the same order as the 2D SLG nonlinear Kerr conductance value. Comparing the isotropic conductances with their anisotropic counterparts, we note similar behavior at

$T = 300\,\mathrm{K}$. These results indicate that for low temperatures, there is a strong enhancement of the third-harmonic nonlinearity; however at room temperature, the Kerr nonlinearity dominates.

Finally, it is worth noting the limitations of our approach. The singularity around the Dirac point in metallic acGNR leads to high mobility, but acGNR can be more prone to edge defects. Furthermore the $\mathbf{k}\cdot\mathbf{p}$ approximation is appropriate only at low energies, well below $2\,\mathrm{eV}$.[46] For Fermi energies greater than optical phonon energy $200\,\mathrm{meV}$, one needs to use a more basic tight-binding description, and the Dirac physics becomes largely irrelevant[46]. For undoped and lightly-doped acGNR, the Fermi energy is well away from these energy scales and the description in terms of the Dirac Hamiltonian should work relatively well. In this paper, we assume there is no coupling of the local nonlinear current density with the spatial distribution of the applied electric field. Further, we treat the metallic acGNR with no applied longitudinal bias voltage, so that the Fermi level does not change across the longitudinal direction of the nanoribbon. It will be important to introduce additional effects in the present model such as the finite extent of the excitation field and the finite longitudinal size of the nanoribbon, as well as material effects such as electron-electron, electron-phonon interactions, and other edge effects. These topics are the subject of our future work.

IV. SELECTION RULES RELATED TO ACGNR

In this section, we discuss the applicability of well-known selection rules for acGNR and 2D SLG to the problem of THz nonlinear harmonic generation in thin metallic acGNR. We focus on the interband transition in the lowest (linear) band ($n = 0$). The fact that we have nonzero g_{yy} and zero g_{xx} is consistent with the selection rules for acGNR found by Sasaki *et.al.*[27] and HC Chung *et.al.*[28]

In general, for 2D SLG there is no anisotropic current (J_y, J_x induced by E_x, E_y). The

anisotropic conductance for intrinsic 2D SLG can be written:

$$
\begin{aligned}
g^{(1)}_{yx}(\omega)_{2D} &= \lim_{\Gamma\to 0} -\frac{g_0}{\pi^2}\int_0^{2\pi}\sin(2\theta)d\theta\int_0^{\infty}\Re\left[i\frac{v_F^2}{\omega^2}\frac{kv_F}{2kv_F-\omega-i\Gamma}k\tanh(\frac{\hbar v_F k}{2k_BT})\right]dk \\
g^{(3)}_{yx}(\omega)_{2D} &= \lim_{\Gamma\to 0}\frac{g_0}{\pi^2}\frac{\eta^2}{2}\int_0^{2\pi}\sin(2\theta)d\theta \\
&\quad\times\int_0^{\infty}\Re\left[i\frac{v_F^2}{\omega^2}\frac{k^2v_F^2[-kv_F+\omega+kv_F\cos(2\theta)]}{[(2kv_F-\omega)^2+\Gamma^2](kv_F-\omega-i\Gamma)}k\tanh(\frac{\hbar v_F k}{2k_BT})\right]dk \\
g^{(3)}_{yx}(3\omega)_{2D} &= \lim_{\Gamma\to 0}\frac{g_0}{\pi^2}\frac{\eta^2}{6}\int_0^{2\pi}\sin(2\theta)d\theta \\
&\quad\times\int_0^{\infty}\Re\left[i\frac{v_F^2}{\omega^2}\frac{kv_F[k^2v_F^2-3kv_F\omega+4\omega^2-k^2v_F^2\cos(2\theta)]}{(2kv_F-\omega-i\Gamma)(kv_F-\omega-i\Gamma)(2kv_F-3\omega-i3\Gamma)}k\tanh(\frac{\hbar v_F k}{2k_BT})\right]dk
\end{aligned}
\tag{28}
$$

where $\eta = \frac{eA_yv_F}{\hbar\omega} = \frac{eE_yv_F}{\hbar\omega^2}$ measures the e-h coupling strengh. Using this result, we see that because $\int_0^{2\pi}\sin(2\theta) = 0$, the conductance terms $g^{(i)}_{yx}(\omega_0)_{2D} = 0$ for 2D SLG. The $g^{(i)}_{xy}(\omega_0)_{2D} = 0$ from similar analysis. The zero anisotropic current in 2D SLG results from that fact that the net sum is zero over all possible angles, and agrees with the quantum analysis performed in Ref.[16] for 2D SLG.

However, as shown above for metallic acGNR, J_ν, $\sigma^{(i)}_{\mu\nu}(m,\omega)$ has the general form:

$$\sigma^{(i)}_{y\nu}(m,\omega) = F^{(i)}_{y\nu}(|k_y|)\cos(\theta_{k_n,k_y}) \tag{29}$$

For metallic acGNR, we no longer integrate all possible angles as we did for 2D SLG. Due to the 1D nature of acGNR, we only have $\theta_{k_n,k_y} = 0,\pi$ depending on the sign of k_y, and thus we only evaluate at two angles according to the initial condition given by Eq. 4 when we evaluate the total current density J_ν for metallic acGNR. As a result, J_ν is not always zero for all E_F, ω and T. For direct interband transitions between states where $k_{x,n} \neq 0$, we make a similar argument as we only require states at $\epsilon = \hbar v_F k_{x,n}\csc(\theta_{k_n,k_y})$ to be at resonance. Thus, we only have the θ_{k_n,k_y} and $\pi - \theta_{k_n,k_y}$ pair as the two solutions. In this way, we extend the selection rules of the direct interband transition for acGNR to the J_x case, *i.e.* $k_{x,n}$ does not change from initial state to final state. This is the same requirement as for J_y in acGNR.

V. CONCLUDING REMARKS

Kimouche *et.al.*[30] and Jacobberger *et.al.*[31] have succesfully fabricated ultrathin, smooth acGNR with widths $L_x < 10\,\text{nm}$. Our calculation of the nonlinear conductance in acGNR

suggest that experimental measurements of the THz nonlinear response in thin metallic acGNR should be measurable at relatively low excitation field strengths. The relatively small critical field strength at room temperature implies that thin metallic acGNR have significant potential for nonlinear device applications. The striking turn on and turn off of the third-order harmonics with small changes in Fermi level at low temperatures suggest that metallic acGNR could be the the basis for developing a sensitive graphene-based low temperature detector or oscillator.

In this paper, we have modeled the third-order THz response of metallic acGNR using a nonlinear semi-analytical approach. The time-dependent Dirac equation for massless Dirac Fermions is solved via the Fourier expansion method. We have shown intrinsic metallic acGNR exhibits strong nonlinear effects from the THz to the FIR regime under applied electric field amplitudes less than 10 kV/m. We also describe the behavior of these nonlinearities for extrinsic, metallic acGNR. Under certain conditions, metallic acGNR will exhibit a larger nonlinear conductance, require less applied electric field strength to generate moderate strong high harmonics and show better temperature stability than intrinsic 2D SLG. This opens the potential for use in many device applications for intrinsic and slightly doping metallic acGNR.

Appendix A: Vector Potential

In the Coulomb gauge, for a constant scalar potential ($\nabla\varphi = 0$), the relationship between the vector potential and the electric field is $E(t) = -\partial A(t)/\partial t$. Thus, for an electric field that is turned on at time t_0, the vector potential is written:

$$A(t) = -\int_{t_0}^{t} E(t_1)\, dt_1 = -E_0 \int_{t_0}^{t} e^{-i\omega t_1}\, dt_1 \tag{A1}$$

Considering a time-harmonic field turned on at $t_0 \to -\infty$, we write the integral in Eq. (A1):

$$\begin{aligned} I &= \int_{-\infty}^{t} e^{-i\omega t_1}\, dt_1 \\ &= \int_{-\infty}^{0} e^{-i\omega t_1}\, dt_1 + \int_{0}^{t} e^{-i\omega t_1}\, dt_1 \\ &= I_1 + I_2 \end{aligned} \tag{A2}$$

In order to evaluate the integral I_1, we introduce an infinitesimally small positive parameter τ, which corresponds to the field turning on adiabatically[36,37] at $-\infty$. With $t' = -t_1$:

$$\begin{aligned} I_1 &= \lim_{\tau\to 0}\int_{-\infty}^{0} e^{(\tau-i\omega)t_1}\,dt_1 \\ &= \lim_{\tau\to 0}\int_{0}^{\infty} e^{-(\tau-i\omega)t'}\,dt' \\ &= \lim_{\tau\to 0}\frac{1}{\tau-i\omega} = \frac{1}{-i\omega} \end{aligned} \tag{A3}$$

Evaluating the integral I_2, we obtain:

$$\begin{aligned} I_2 &= \int_{0}^{t} e^{-i\omega t}\,dt_1 \\ &= \frac{e^{-i\omega t}-1}{-i\omega} \end{aligned} \tag{A4}$$

The total integral I is obtained by summing I_1 and I_2:

$$I = I_1 + I_2 = \frac{1}{-i\omega} + \frac{e^{-i\omega t}-1}{-i\omega} = \frac{e^{-i\omega t}}{-i\omega} \tag{A5}$$

and the vector potential in the Coulomb gauge for a time-harmonic electric field that turns on adiabatically at $t_0 \to -\infty$ becomes:

$$A(t) = -E_0 I = \frac{-E_0 e^{-i\omega t}}{-i\omega} = \frac{E(t)}{i\omega} \tag{A6}$$

Appendix B: Derivation of the 2D SLG Nonlinear Conductance

Following Wright, *et.al.*[11] and Ang *et.al.*[21], we compute the third-order current densities for 2D SLG due to an $\hat{x}$-polarized electric field of the form $\hat{x}E_0e^{i\omega t}$. Defining $p = \sqrt{p_x^2+p_y^2}$, and $\tan(\theta) = \frac{p_y}{p_x}$, and using the fact that $\int_0^{2\pi}\cos(2\theta)d\theta = \int_0^{2\pi}\sin(2\theta)d\theta = \int_0^{2\pi}\cos(4\theta)d\theta = \int_0^{2\pi}\sin(4\theta)d\theta = 0$ the current densities in the $\hat{x}$ direction are written[11–13,21,25,40–42]:

$$J_3^x(\omega) = \lim_{\Gamma\to 0}\frac{g_s g_v}{(2\pi\hbar)^2} g_0\eta\int_0^{2\pi} d\theta\int_0^{\infty}\Re\left\{ i\frac{-v_F^2(3p^3v_F^3 - 8\hbar p^2 v_F^2\hbar\omega + 6pv_F\hbar^2\omega^2 - 2\hbar^3\omega^3)N(p)p}{\omega^2[2pv_F-\hbar(\omega+i\Gamma)][2pv_F-\hbar(\omega-i\Gamma)][pv_F-\hbar(\omega+i\Gamma)]}\right\} dp \tag{B1}$$

$$J_3^x(3\omega) = \lim_{\Gamma\to 0}\frac{g_s g_v}{(2\pi\hbar)^2} g_0\eta\int_0^{2\pi} d\theta\int_0^{\infty}\Re\left\{ i\frac{v_F^2(3p^3v_F^3 - 12\hbar p^2 v_F^2\hbar\omega + 14pv_F\hbar^2\omega^2 - 6\hbar^3\omega^3)N(p)p}{3\omega^2[2pv_F-\hbar(\omega+i\Gamma)][pv_F-\hbar(\omega+i\Gamma)][2pv_F-3\hbar(\omega+i\Gamma)]}\right\} dp \tag{B2}$$

with g_s, $g_v = 2$, $g_0 = \frac{e^2}{4\hbar}$, $\eta = \frac{e^2E_0^2v_F^2}{\hbar^2\omega^4}$, and $N(p) = \tanh(\frac{pv_F}{2k_BT})$.

In these expressions, the integrands are of the form:

$$i_1(x) = f_1(x)\Re\left[i\frac{1}{(2x - x_0 - i\Gamma)(2x - x_0 + i\Gamma)(x - x_0 - i\Gamma)}\right] \tag{B3}$$

$$i_3(x) = f_3(x)\Re\left[i\frac{1}{(2x - x_0 - i\Gamma)(x - x_0 - i\Gamma)(2x - 3x_0 - i3\Gamma)}\right] \tag{B4}$$

for the Kerr and third-order currents respectively, with $f_1(x)$, $f_3(x)$, x_0, Γ real. After some algebra we find that these integrands become:

$$i_1(x) = f_1(x)\frac{\pi}{x\,(3x - 2x_0)}\left[\frac{1}{\pi}\frac{\Gamma}{(2x - x_0)^2 + \Gamma^2} - \frac{1}{\pi}\frac{\Gamma}{(x - x_0)^2 + \Gamma^2}\right] \tag{B5a}$$

$$i_3(x) = f_3(x)\frac{\pi}{x^2}\left[-\frac{1}{4}\frac{1}{\pi}\frac{\Gamma}{(2x - x_0)^2 + \Gamma^2} + \frac{1}{\pi}\frac{\Gamma}{(x - x_0)^2 + \Gamma^2} - \frac{9}{4}\frac{1}{\pi}\frac{3\Gamma}{(2x - 3x_0)^2 + 9\Gamma^2}\right] \tag{B5b}$$

As a result, the expressions for the current density in Eqs. (B1) and (B2) above may be expanded as a set of integrals of the form:

$$Z_1 = \lim_{\Gamma\to 0}\int_a^b \Re\left[\frac{iz(x)}{x - x_0 \mp i\Gamma}\right]\,dx = \lim_{\Gamma\to 0}\int_a^b \Re\left[z_1(x, x_0, \Gamma)\right]\,dx \tag{B6}$$

with $z(x)$, x, x_0, $\Gamma > 0$ real. Using the property:

$$\lim_{\Gamma\to 0}\frac{1}{\pi}\frac{\Gamma}{(x - x_0)^2 + \Gamma^2} = \delta(x - x_0) \tag{B7}$$

we arrive at $Z_1 = \pi f(x_0)$. Several example problems involving this type of kernel may be found in Refs.[47–50].

Alternatively, we may use the Cauchy Principal Value theorem to solve this problem. Separating the real and imaginary parts of the integrand $z_1(x, x_0, \Gamma)$, we obtain:

$$\Re\left[z_1(x, x_0, \Gamma)\right] = \mp\pi\frac{1}{\pi}\frac{\Gamma}{(x - x_0)^2 + \Gamma^2}z(x) \tag{B8}$$

$$\Im\left[z_1(x, x_0, \Gamma)\right] = \frac{1}{(x - x_0) + \Gamma^2/\,(x - x_0)}z(x) \tag{B9}$$

The Sokhotsky-Plemelj theorem on the real interval $[a, b]$ states[51]:

$$\lim_{\Gamma\to 0}\int_a^b \frac{g(x)}{x - x_0 \mp i\Gamma}dx = \mathbb{P}\int_a^b \frac{g(x)}{x - x_0}dx \pm i\pi g(x_0) \tag{B10}$$

where $\mathbb{P}\int_a^b g(x)dx$ denotes the Cauchy principal integral of $g(x)$. For $g(x) = iz(x)$ with $z(x)$ real, the real and imaginary parts become:

$$\Re\left[\lim_{\Gamma\to 0}\int_a^b \frac{iz(x)}{x - x_0 \mp i\Gamma}\,dx\right] = \mp\pi z(x_0) \tag{B11}$$

$$\Im\left[\lim_{\Gamma\to 0}\int_a^b \frac{iz(x)}{x - x_0 \mp i\Gamma}\,dx\right] = \mathbb{P}\int_a^b \frac{z(x)}{x - x_0}dx \tag{B12}$$

which is the same result as in Eq. (B7).

An analysis of the interband transition using the Kubo formula has appeared in Ref.[38]. Eq. (A1) of that reference further confirms our result for 2D SLG.

Based on the above analysis, in the limit as $\Gamma \to 0$, the integrands in Eq. (B5) reduce to:

$$\lim_{\Gamma\to 0} i_1(x) = \frac{\pi f_1(x)}{x(3x-2x_0)}\left[\frac{\delta(x-\frac{x_0}{2})}{2} - \delta(x-x_0)\right]$$
$$= -\frac{\pi f_1(x)}{x_0^2}\left[2\delta(x-\frac{x_0}{2}) + \delta(x-x_0)\right] \tag{B13}$$

$$\lim_{\Gamma\to 0} i_3(x) = \frac{\pi f_3(x)}{x^2}\left[-\frac{1}{4}\frac{\delta(x-\frac{x_0}{2})}{2} + \delta(x-x_0) - \frac{9}{4}\frac{\delta(x-\frac{3x_0}{2})}{2}\right] \tag{B14}$$

and the integrals reduce to:

$$I_1 = -\frac{\pi}{x_0^2}[2f_1(\frac{x_0}{2}) + f_1(x_0)] \tag{B15}$$

$$I_3 = -\frac{\pi}{2x_0^2}\left[f_3(\frac{x_0}{2}) - 2f_3(x_0) + f_3(\frac{3x_0}{2})\right] \tag{B16}$$

Therefore, the current densities may be written:

$$J_3^x(\omega) = -g_0 E_0 \frac{e^2E_0^2v_F^2}{\hbar^2\omega^4}\left[\frac{5}{4}\tanh(\frac{\hbar\omega}{4k_BT}) + 2\tanh(\frac{\hbar\omega}{2k_BT})\right] \tag{B17}$$

$$J_3^x(3\omega) = g_0 E_0 \frac{e^2E_0^2v_F^2}{\hbar^2\omega^4}\left[\frac{13}{48}\tanh(\frac{\hbar\omega}{4k_BT}) - \frac{2}{3}\tanh(\frac{\hbar\omega}{2k_BT}) + \frac{45}{48}\tanh(\frac{3\hbar\omega}{4k_BT})\right] \tag{B18}$$

resulting in the Kerr conductance:

$$g_{xx}^{(3)}(\omega)_{2D} = -g_0 \frac{e^2E_0^2v_F^2}{\hbar^2\omega^4}\left[\frac{5}{4}\tanh(\frac{\hbar\omega}{4k_BT}) + 2\tanh(\frac{\hbar\omega}{2k_BT})\right] \tag{B19}$$

and the third-harmonic conductance:

$$g_{xx}^{(3)}(3\omega)_{2D} = g_0 \frac{e^2E_0^2v_F^2}{\hbar^2\omega^4}\left[\frac{13}{48}\tanh(\frac{\hbar\omega}{4k_BT}) - \frac{2}{3}\tanh(\frac{\hbar\omega}{2k_BT}) + \frac{45}{48}\tanh(\frac{3\hbar\omega}{4k_BT})\right] \tag{B20}$$

Similarly, for a $\hat{y}$-polarized electric field of the form $\hat{y}E_0e^{i\omega t}$, we arrive at an identical result for the third-order Kerr current in the $\hat{y}$ direction, or equivalently $g_{xx}^{(3)}(\omega) = g_{yy}^{(3)}(\omega)$ and $g_{xx}^{(3)}(3\omega) = g_{yy}^{(3)}(3\omega)$ for 2D SLG.

A comparison of Eqs. (23) and (24) for intrinsic 2D SLG with $E_0 = 10\,\mathrm{kV/m}$ at $T = 0\,\mathrm{K}$ and $300\,\mathrm{K}$ is plotted in Fig. 8. This shows that while small, the correction due to the $\omega/2$ resonant term is certainly not negligible.

To further amplify our point that there are two terms in the expression for the third-order Kerr nonlinear conductance, we note that Eq. 33 may also be written as:

$$\begin{aligned} i_1(x) &= f_1(x)\Re\left[i\frac{1}{(2x-x_0-i\Gamma)(2x-x_0+i\Gamma)(x-x_0-i\Gamma)}\right] \\ &= -f_1(x)\left[\frac{1}{(2x-x_0)^2+\Gamma^2}\right]\left[\frac{\Gamma}{(x-x_0)^2+\Gamma^2}\right] \\ &= -\frac{f_1(x)\Gamma}{4}\left[\frac{1}{(x-a_1x_0)^2+(a_1\Gamma)^2}\right]\left[\frac{1}{(x-a_2x_0)^2+(a_2\Gamma)^2}\right] \end{aligned} \tag{B21}$$

with $a_1 = 1/2, a_2 = 1$. Eq. B21 is symmetric in (a_1, a_2), and therefore the integral I_1 must also be symmetric in (a_1, a_2). Thus, both $\omega/2$ and ω terms must appear in the expression for the Kerr conductance, Eq. B19.

---

[1] D. Abergel, V. Apalkov, J. Berashevich, K. Ziegler, and T. Chakraborty, Adv. Phys. **59**, 261 (2010).

[2] R. Nair, P. Blake, A. Grigorenko, K. Novoselov, T. Booth, T. Stauber, N. Peres, and A. Geim, Science **320**, 1308 (2008).

[3] S. Mikhailov, Europhys. Lett. **79**, 27002 (2007).

[4] E. Hendry, P. J. Hale, J. Moger, A. K. Savchenko, and S. A. Mikhailov, Phys. Rev. Lett. **105**, 097401 (2010).

[5] T. Gu, N. Petrone, J. F. McMillan, A. van der Zande, M. Yu, G.-Q. Lo, D.-L. Kwong, J. Hone, and C. W. Wong, Nat. Photonics **6**, 554 (2012).

[6] M. Glazov and S. Ganichev, Physics Reports **535**, 101 (2014).

[7] A. C. Neto, F. Guinea, N. Peres, K. S. Novoselov, and A. K. Geim, Rev. Mod. Phys. **81**, 109 (2009).

[8] S. D. Sarma, S. Adam, E. Hwang, and E. Rossi, Rev. Mod. Phys. **83**, 407 (2011).

[9] S. Mikhailov and K. Ziegler, J. Phys.: Condens. Matter **20**, 384204 (2008).

[10] S. Mikhailov, Physica E **44**, 924 (2012).

[11] A. Wright, X. Xu, J. Cao, and C. Zhang, Appl. Phys. Lett. **95**, 072101 (2009).

[12] Y. S. Ang, S. Sultan, and C. Zhang, Appl. Phys. Lett. **97**, 243110 (2010).

[13] Y. S. Ang and C. Zhang, Appl. Phys. Lett. **98**, 042107 (2011).

[14] M. Gullans, D. E. Chang, F. H. L. Koppens, F. J. Garcia deAbajo, and M. D. Lukin, Phys. Rev. Lett. **111**, 247401 (2013).

[15] S. A. Mikhailov, Phys. Rev. B **90**, 241301(R) (2014); **91**, 039904(E) (2015).

[16] S. A. Mikhailov, Phys. Rev. B **93**, 085403 (2016).

[17] J. L. Cheng, N. Vermeulen, and J. E. Sipe, New J. Phys. **16**, 053014 (2014); **18**, 029501(E) (2016).

[18] J. L. Cheng, N. Vermeulen, and J. E. Sipe, Phys. Rev. B **92**, 235307 (2015).

[19] J. L. Cheng, N. Vermeulen, and J. E. Sipe, Phys. Rev. B **91**, 235320 (2015); **93**, 039904(E) (2016).

[20] T. Morimoto and N. Nagaosa, Phys. Rev. B **93**, 125125 (2016).

[21] Y. S. Ang, Q. Chen, and C. Zhang, Frontiers of Optoelectronics **8**, 3 (2015).

[22] N. Kumar, J. Kumar, C. Gerstenkorn, R. Wang, H.-Y. Chiu, A. L. Smirl, and H. Zhao, Phys. Rev. B **87**, 121406 (2013).

[23] I. Maeng, S. Lim, S. J. Chae, Y. H. Lee, H. Choi, and J.-H. Son, Nano Lett. **12**, 551 (2012).

[24] H. A. Hafez, I. Al-Naib, M. M. Dignam, Y. Sekine, K. Oguri, F. Blanchard, D. G. Cooke, S. Tanaka, F. Komori, H. Hibino, *et al.*, Phys. Rev. B **91**, 035422 (2015).

[25] Q. Bao and K. P. Loh, ACS Nano **6**, 3677 (2012).

[26] Z. Duan, W. Liao, and G. Zhou, Advances in Condensed Matter Physics **2010** (2010).

[27] K. I. Sasaki, K. Kato, Y. Tokura, K. Oguri, and T. Sogawa, Phys. Rev. B **84**, 085458 (2011).

[28] H. Chung, M. Lee, C. Chang, and M. Lin, Opt. Express **19**, 23350 (2011).

[29] X. Wang, Y. Ouyang, L. Jiao, H. Wang, L. Xie, J. Wu, J. Guo, and H. Dai, Nat. Nanotechnol. **6**, 563 (2011).

[30] A. Kimouche, M. M. Ervasti, R. Drost, S. Halonen, A. Harju, P. M. Joensuu, J. Sainio, and P. Liljeroth, Nat. Commun. **6** (2015).

[31] R. M. Jacobberger, B. Kiraly, M. Fortin-Deschenes, P. L. Levesque, K. M. McElhinny, G. J. Brady, R. R. Delgado, S. S. Roy, A. Mannix, M. G. Lagally, *et al.*, Nat. Commun. **6** (2015).

[32] L. Brey and H. A. Fertig, Phys. Rev. B **73**, 235411 (2006).

[33] L. Brey and H. A. Fertig, Phys. Rev. B **75**, 125434 (2007).

[34] D. R. Andersen and H. Raza, Phys. Rev. B **85**, 075425 (2012).

[35] D. R. Andersen and H. Raza, J. Phys.: Condens. Matter **25**, 045303 (2013).

[36] G. D. Mahan, *Many-Particle Physics* (Springer Science & Business Media, 2000).

[37] S. Ryu, C. Mudry, A. Furusaki, and A. W. W. Ludwig, Phys. Rev. B **75**, 205344 (2007).

[38] M. V. Strikha and F. T. Vasko, Phys. Rev. B **81**, 115413 (2010).

[39] S. Winnerl, F. Göttfert, M. Mittendorff, H. Schneider, M. Helm, T. Winzer, E. Malic, A. Knorr, M. Orlita, M. Potemski, *et al.*, J. of Phys.: Condens. Matter **25**, 054202 (2013).

[40] F. J. Lopez-Rodriguez and G. G. Naumis, Phys. Rev. B **78**, 201406 (2008).

[41] Y. Zhou and M. W. Wu, Phys. Rev. B **83**, 245436 (2011).

[42] E. G. Mishchenko, Phys. Rev. Lett. **103**, 246802 (2009).

[43] M. Arons, M. Han, and E. Sudarshan, Phys. Rev. **137**, B1085 (1965).

[44] J. Tworzydło, B. Trauzettel, M. Titov, A. Rycerz, and C. W. J. Beenakker, Phys. Rev. Lett. **96**, 246802 (2006).

[45] H. Nasari, M. S. Abrishamian, and P. Berini, Opt. Express **24**, 708 (2016).

[46] H. Raza, *Graphene nanoelectronics: Metrology, synthesis, properties and applications* (2012).

[47] L. Caffarelli and L. Silvestre, Commun. Part. Diff. Eq. **32**, 1245 (2007).

[48] G. Wei, Y. Zhao, and Y. Xiang, Int. J. Numer. Meth. Eng. **55**, 913 (2002).

[49] M. G. Katz and D. Tall, Found. Sci. **18**, 107 (2013).

[50] X. Liu, X. Jin, J.-H. Lee, L. Zhu, H.-I. Kwon, and J.-H. Lee, Semicond. Sci. Tech. **25**, 015008 (2010).

[51] V. S. Vladimirov, *Equations of Mathematical Physics* (Marcel Dekker, New York, 1971).

[52] K. L. Ishikawa, Phys. Rev. B **82**, 201402 (2010).

[53] S. Winnerl, M. Orlita, P. Plochocka, P. Kossacki, M. Potemski, T. Winzer, E. Malic, A. Knorr, M. Sprinkle, C. Berger, *et al.*, Phys. Rev. Lett. **107**, 237401 (2011).

[54] J. H. Strait, H. Wang, S. Shivaraman, V. Shields, M. Spencer, and F. Rana, Nano Lett. **11**, 4902 (2011).

[55] J. C. Johannsen, S. Ulstrup, F. Cilento, A. Crepaldi, M. Zacchigna, C. Cacho, I. E. Turcu, E. Springate, F. Fromm, C. Raidel, *et al.*, Phys. Rev. Lett. **111**, 027403 (2013).

[56] I. Gierz, J. C. Petersen, M. Mitrano, C. Cacho, I. E. Turcu, E. Springate, A. Stöhr, A. Köhler, U. Starke, and A. Cavalleri, Nat. Mater. **12**, 1119 (2013).

[57] P. A. George, J. Strait, J. Dawlaty, S. Shivaraman, M. Chandrashekhar, F. Rana, and M. G. Spencer, Nano Lett. **8**, 4248 (2008).

[58] G. Jnawali, Y. Rao, H. Yan, and T. F. Heinz, Nano Lett. **13**, 524 (2013).

[59] Y. Yang and R. Murali, IEEE Electr. Device L. **31**, 237 (2010).

[60] A. D. Liao, J. Z. Wu, X. Wang, K. Tahy, D. Jena, H. Dai, and E. Pop, Phys. Rev. Lett. **106**, 256801 (2011).

[61] S. Thongrattanasiri, A. Manjavacas, and F. J. Garca de Abajo, ACS Nano **6**, 1766 (2012).

[62] P. N. Romanets and F. T. Vasko, Phys. Rev. B **81**, 085421 (2010).

[63] W.-K. Tse and S. Das Sarma, Phys. Rev. B **79**, 235406 (2009).

[64] H. Shen, Y. Shi, and X. Wang, Synth. Met. **210**, 109 (2015).

[65] D. Bischoff, A. Varlet, P. Simonet, M. Eich, H. Overweg, T. Ihn, and K. Ensslin, Appl. Phys. Rev. **2**, 031301 (2015).

[66] I. S. Gradshteyn and I. M. Ryzhik, *Table of integrals, series, and products*, 8th ed., edited by D. Zwillinger (Elsevier, 2014).

[67] J. D. Jackson, *Classical electrodynamics*, 3rd ed. (Wiley, 1999).

[68] I. Brihuega, P. Mallet, C. Bena, S. Bose, C. Michaelis, L. Vitali, F. Varchon, L. Magaud, K. Kern, and J.-Y. Veuillen, Phys. Rev. Lett. **101**, 206802 (2008).

[69] G. Rutter, J. N. Crain, N. P. Guisinger, T. Li, P. N. First, and J. A. Stroscio, Science **317**, 219 (2007).

[70] Z. Liu, M. Sanderson, C. Zhang, and J. C. Cao, J. Appl. Phys. **118**, 043106 (2015).

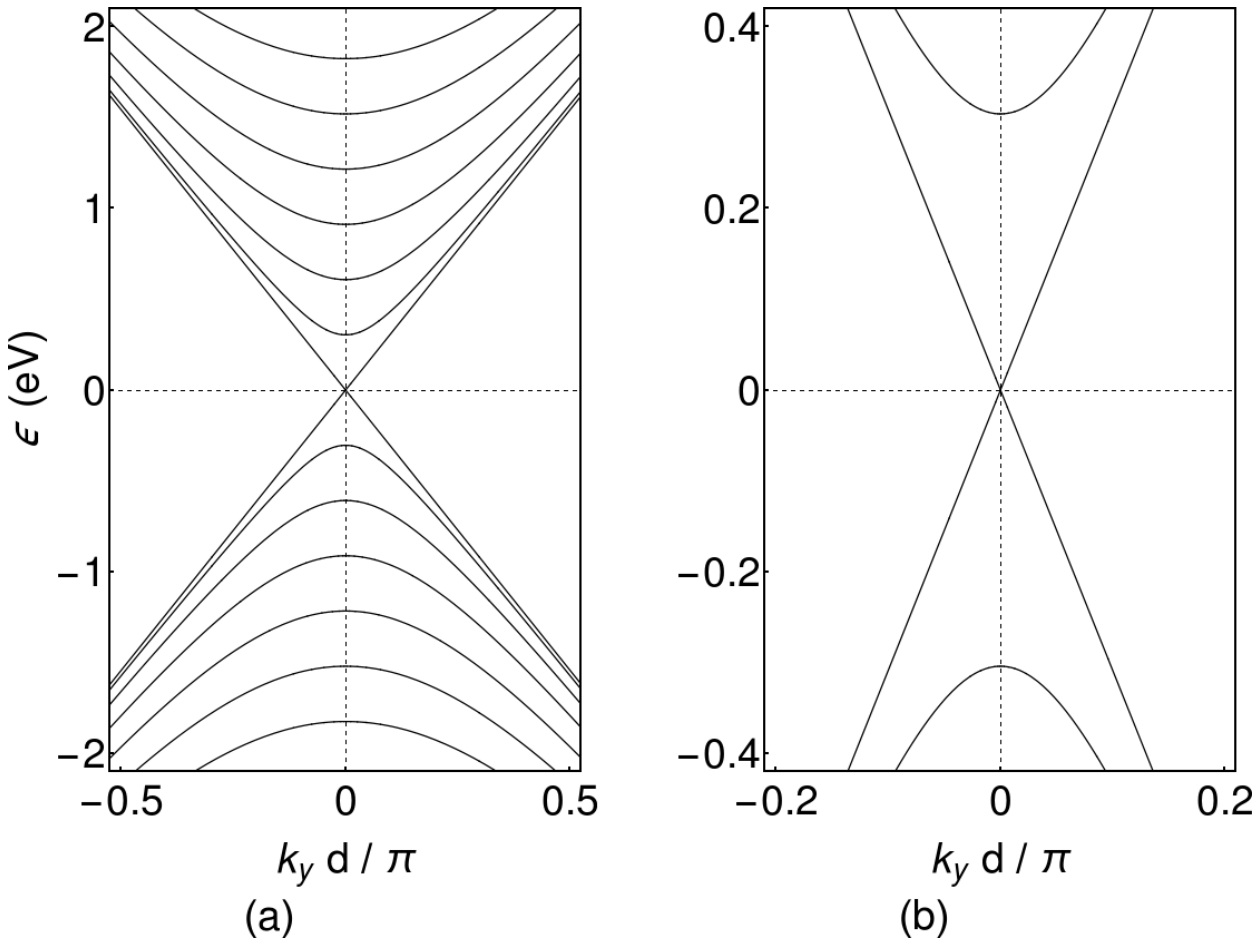

FIG. 1. $\mathbf{k}\cdot\mathbf{p}$ band structure of infinitely long metallic acGNR of width $L_x = 24.6$Å (acGNR20) and $L_y \to \infty$. (a) illustrates the seven lowest-energy bands, and (b) illustrates the gap of $\sim 608\,\text{meV}$ between $n = 1$ conduction and valence band. Here d is the width of the acGNR unit cell ($d = (1+\sqrt{3})a_{cc}$).

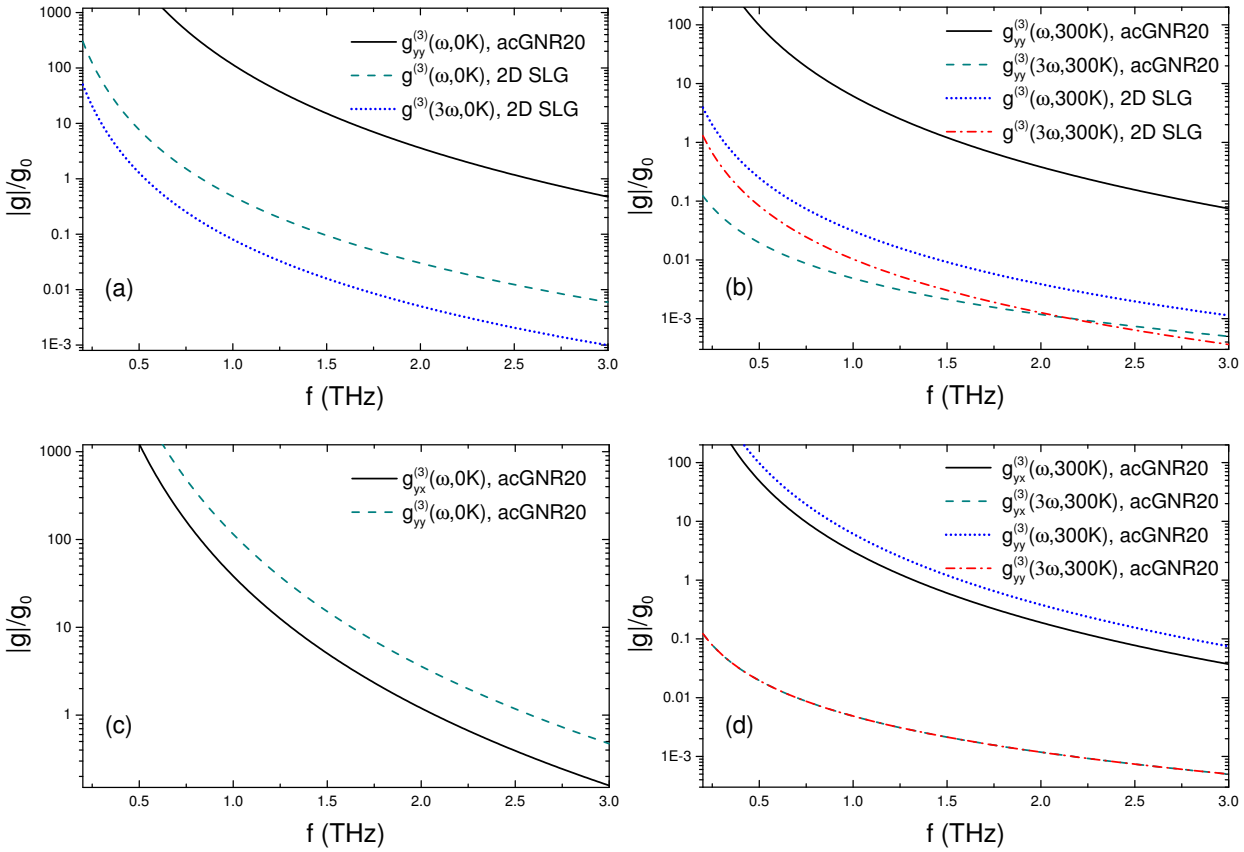

FIG. 2. (color online) Comparison of the Kerr and third-harmonic nonlinear conductances for intrinsic acGNR20 with 2D SLG at (a) $T = 0\,\mathrm{K}$ and (b) $T = 300\,\mathrm{K}$; and comparison of isotropic and anisotropic conductances for acGNR20 at (c) $T = 0\,\mathrm{K}$ and (d) $T = 300\,\mathrm{K}$. The field strength used in all calculations is $E_y = 10\,\mathrm{kV/m}$ and the excitation frequency $f = \omega/2\pi$.

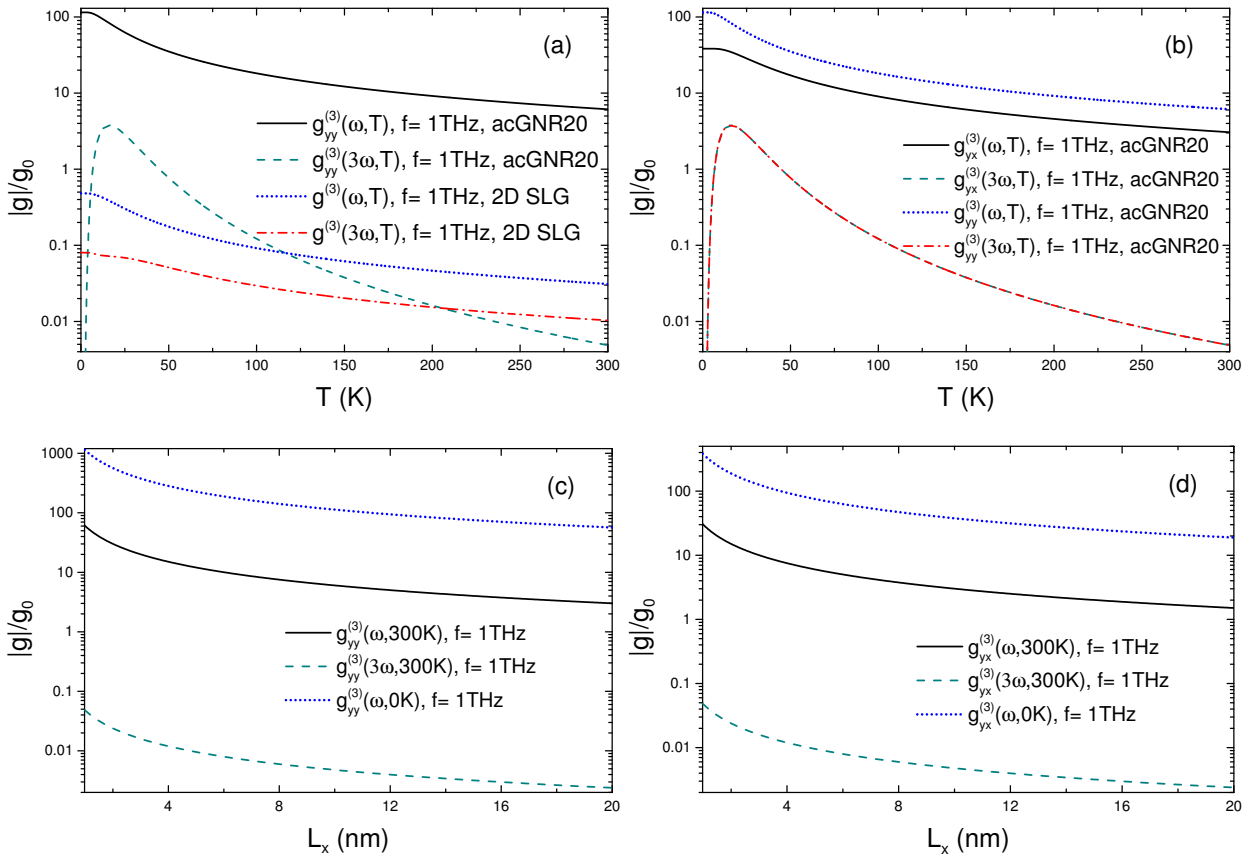

FIG. 3. (color online) Comparison of the temperature dependence of the Kerr and third-harmonic nonlinear conductances for (a) intrinsic acGNR20 with that of 2D SLG; (b) isotropic and anisotropic nonlinear conductances for intrinsic acGNR20; comparison of the nanoribbon width dependence of (c) the Kerr and third-harmonic isotropic nonlinear conductances; and (d) the Kerr and third-harmonic anisotropic nonlinear conductance. The excitation frequency used in all calculations is $f = \omega/2\pi = 1\,\mathrm{THz}$.

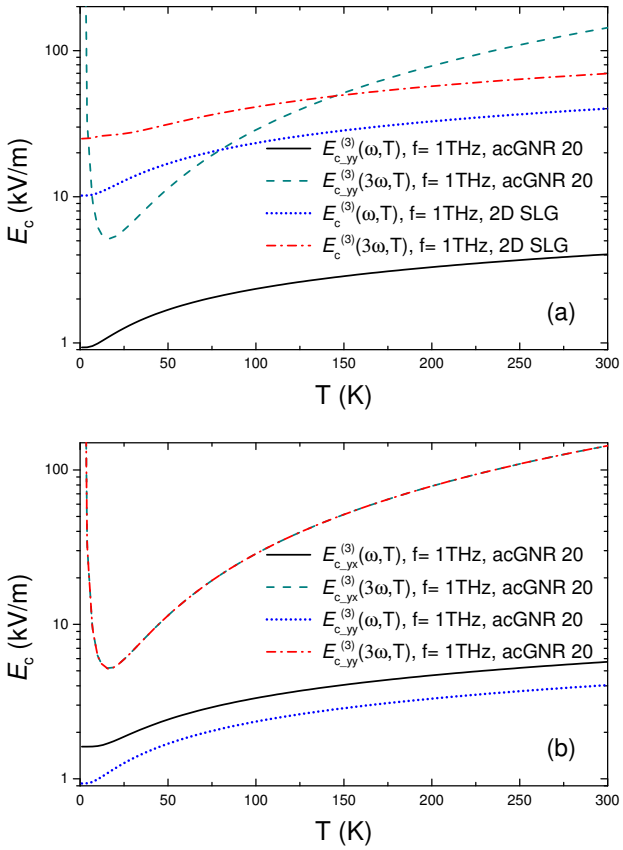

FIG. 4. (color online) Comparison of the temperature dependence of the critical fields for (a) the isotropic Kerr and third-harmonic processes for intrinsic acGNR20 with those of 2D SLG; and (b) the isotropic and anisotropic Kerr and third-harmonic nonlinear processes for intrinsic acGNR20. The excitation frequency used in all calculations is $f = \omega/2\pi = 1\,\mathrm{THz}$.

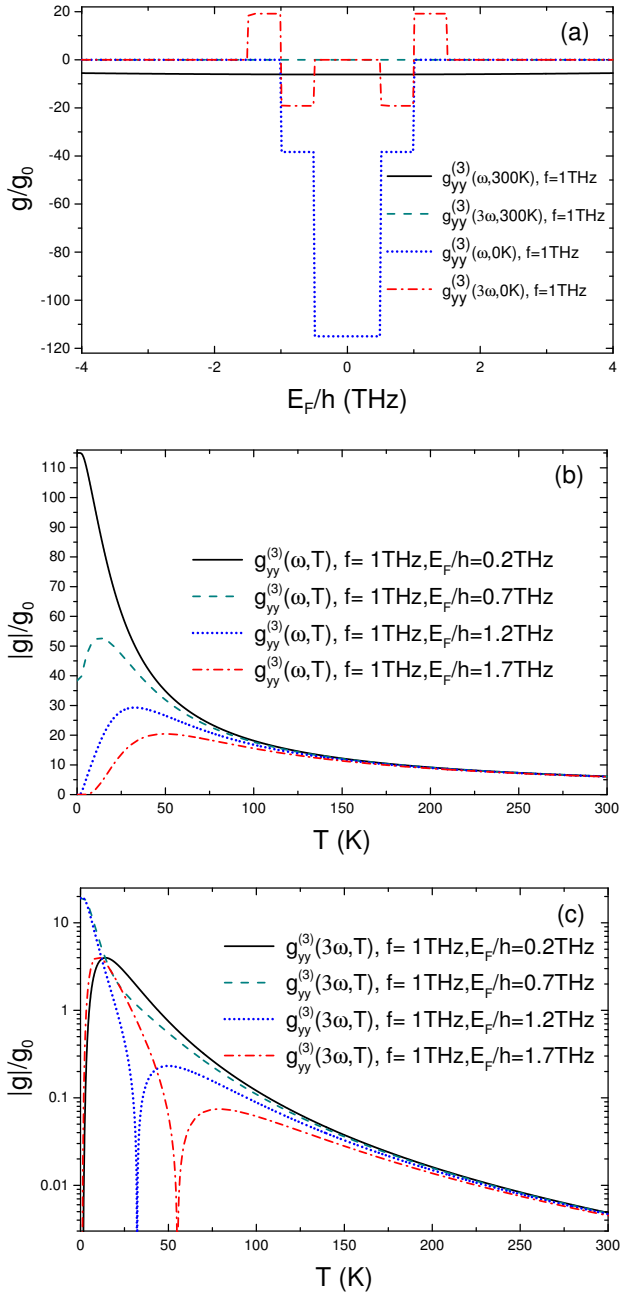

FIG. 5. (color online) (a) The E_F dependence of the isotropic Kerr and third-order nonlinear conductances of acGNR20 at $T = 0\,\mathrm{K}$ and $T = 300\,\mathrm{K}$; (b) the temperature dependence of the isotropic Kerr nonlinear conductance of acGNR20 for various Fermi levels; and (c) the temperature dependence of the isotropic third-harmonic nonlinear conductances of acGNR20 for various Fermi levels. The excitation frequency used in all calculations is $f = \omega/2\pi = 1\,\mathrm{THz}$.

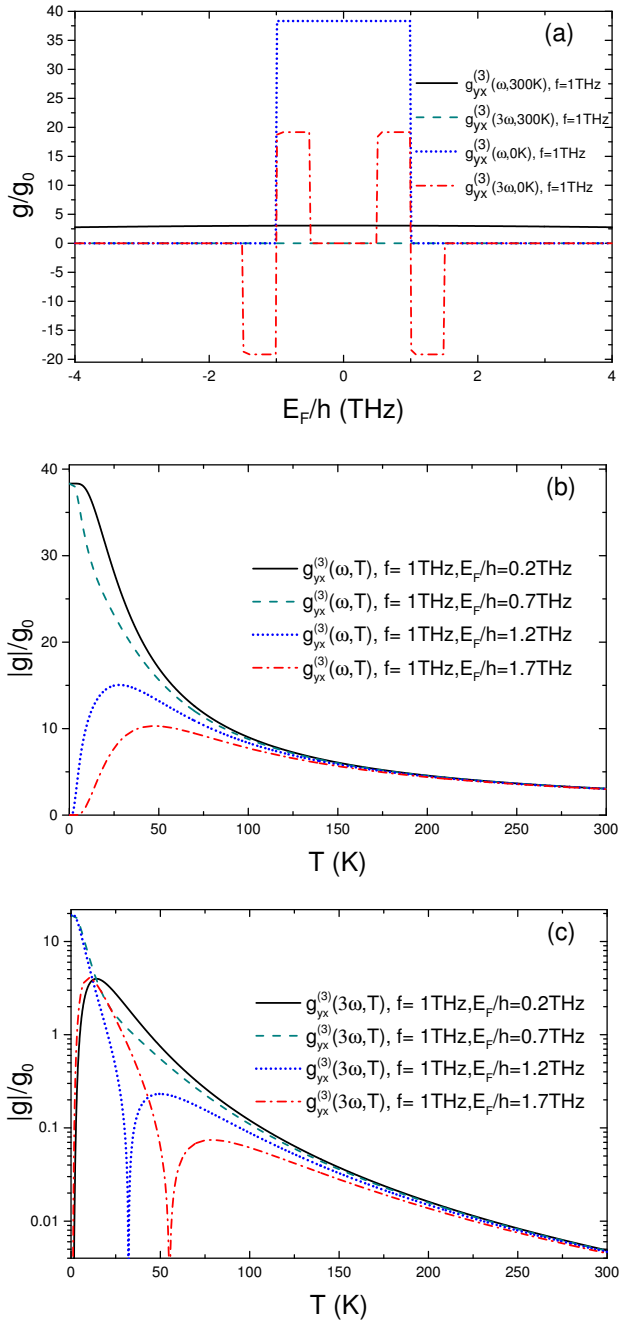

FIG. 6. (color online) (a) The E_F dependence of the anisotropic Kerr and third-order nonlinear conductances of acGNR20 at $T = 0\,\mathrm{K}$ and $T = 300\,\mathrm{K}$; (b) the temperature dependence of the anisotropic Kerr nonlinear conductances of acGNR20 for various Fermi levels; and (c) the temperature dependence of the anisotropic third-harmonic nonlinear conductances of acGNR20 for various Fermi levels. The excitation frequency used in all calculations is $f = \omega/2\pi = 1\,\mathrm{THz}$.

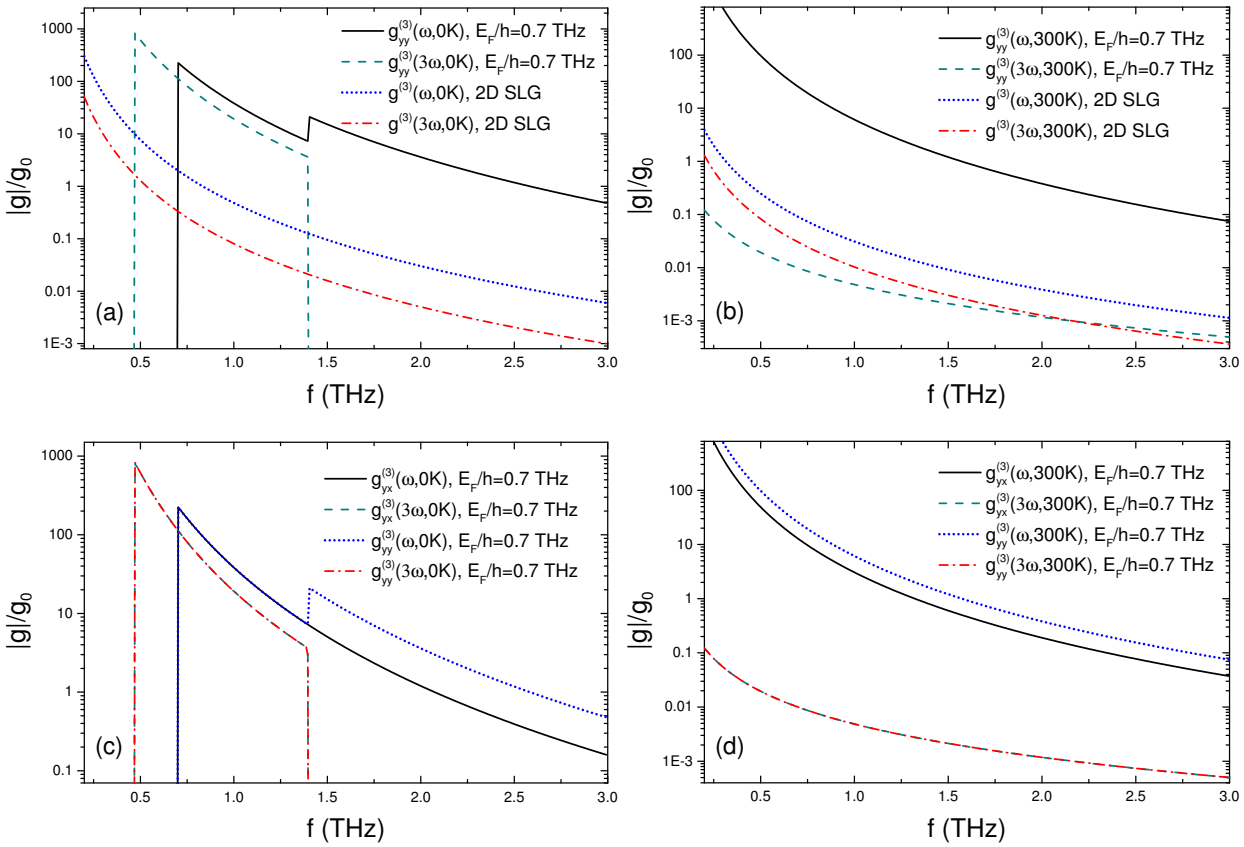

FIG. 7. (color online) Comparison of isotropic Kerr and third-harmonic nonlinearities of extrinsic acGNR20 ($E_F/h = 0.7\,\mathrm{THz}$) at (a) $T = 0\,\mathrm{K}$; and (b) $T = 300\,\mathrm{K}$ with those of intrinsic 2D SLG; and comparison of isotropic and anisotropic Kerr and third-harmonic nonlinearities of extrinsic acGNR20 ($E_F/h = 0.7\,\mathrm{THz}$) at (c) $T = 0\,\mathrm{K}$; and (d) $T = 300\,\mathrm{K}$. The field strength used in all calculations is $E_y = 10\,\mathrm{kV/m}$ and the excitation frequency $f = \omega/2\pi$.

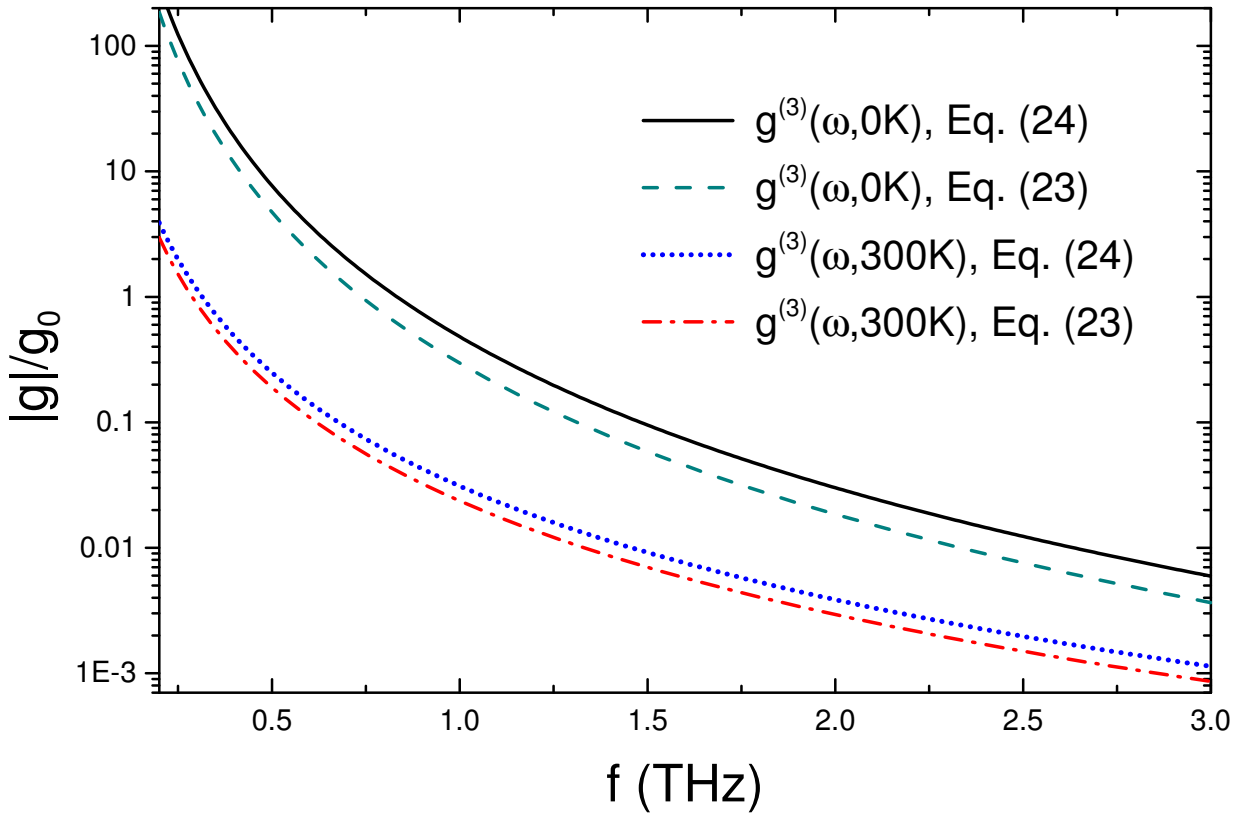

FIG. 8. (color online) Comparison of the third-order nonlinear conductance of for intrinsic 2D SLG from Eqs. (23) and (24) at $T = 0\,\mathrm{K}$ and $300\,\mathrm{K}$. The field strength used in all calculations is $E_0 = 10\,\mathrm{kV/m}$ and the excitation frequency $f = \omega/(2\pi)$.